Geophys. J. Int. (2002) **150,** 610–638

A wavelet-based method for simulation of two-dimensional elastic wave propagation

Tae-Kyung Hong and B. L. N. Kennett

Research School of Earth Sciences, Institute of Advanced Studies, The Australian National University, Canberra ACT 0200, *Australia*
E-mails: tkhong@rses.anu.edu.au; brian@rses.anu.edu.au

Accepted 2002 February 25. Received 2001 October 8; in original form 2001 March 9

SUMMARY

A wavelet-based method is introduced for the modelling of elastic wave propagation in 2-D media. The spatial derivative operators in the elastic wave equations are treated through wavelet transforms in a physical domain. The resulting second-order differential equations for time evolution are then solved via a system of first-order differential equations using a displacement-velocity formulation. With the combined aid of a semi-group representation and spatial differentiation using wavelets, a uniform numerical accuracy of spatial differentiation can be maintained across the domain. Absorbing boundary conditions are considered implicitly by including attenuation terms in the governing equations and the traction-free boundary condition at a free surface is implemented by introducing equivalent forces in the semi-group scheme. The method is illustrated by application to *SH* and *P–SV* waves for several models and some numerical results are compared with analytical solutions. The wavelet-based method achieves a good numerical simulation and shows an applicability for an elastic-wave study.

Key words: elastic waves, numerical modelling, propagation, semi-group, wavelet transform, wavelets.

1 INTRODUCTION

The use of synthetic seismograms is one of most useful methods in estimating the seismic response of media at a given receiver. Various numerical approaches have been proposed to solve the elastic wave equations. For problems related to a stratified medium, the reflectivity method (Kennett 1983) provides a useful means of modelling the seismic response out to the long distances. By taking a Fourier transform with respect to time and introducing a composite use of a Hankel transform and Fourier transform to horizontal components, Kennett (1983) recast the elastic wave equations in terms of a system of the first-order differential equations for the vertical direction and then superposed the cylindrical waves in stratified media to determine the response at a receiver.

For more complex media, various methods have been introduced. The finite difference (FD) method (Kelly *et al.* 1976; Virieux 1986) is applicable to many problems in simple media because the FD scheme is relatively easy to implement in computer codes and does not requires too much computer time and memory. However, the FD scheme encounters difficulties when it is applied to problems such as laterally heterogeneous media with irregular non-planar boundaries or media with free surface topography (e.g. Moczo 1998). Therefore, special care is needed to implement the boundary conditions. Moczo *et al.* (1997) combined the finite difference and finite element (FE) methods near the free surface, since it is much easier to satisfy the boundary conditions in the FE scheme. The pseudo-spectral method based on Chebychev expansions can provide higher accuracy spatial differentiation than simple FD or FE methods by using a series of global, infinitely differentiable basis functions (Augenbaum 1992; Kosloff *et al.* 1990). However, this style of pseudo-spectral method suffers from a nonuniform grid spacing for the collocation points of the basis functions. The non-uniform grid spacing problem requires an increase in the number of grid points to remove grid dispersion and makes it difficult to handle complicated geometries. Recently the spectral element method (SEM) was introduced for various media problems (Faccioli *et al.* 1996; Komatitsch & Vilotte 1998; Komatitsch & Tromp 1999). By including boundary conditions in a variational form of the governing equations and using element interaction, Komatitsch & Vilotte (1998) satisfied the free-surface boundary condition directly and so avoided one of the usual complications in numerical work.

We introduce a wavelet-based method for numerical simulation of elastic wave propagation. In this method we represent the differential operators via multiscale wavelets, and can achieve high accuracy in the spatial representation. The scheme does not require a non-uniform grid as in the Chebychev implementation of the pseudo-spectral method and can be adapted to a wide range of media geometries and related phenomenon.

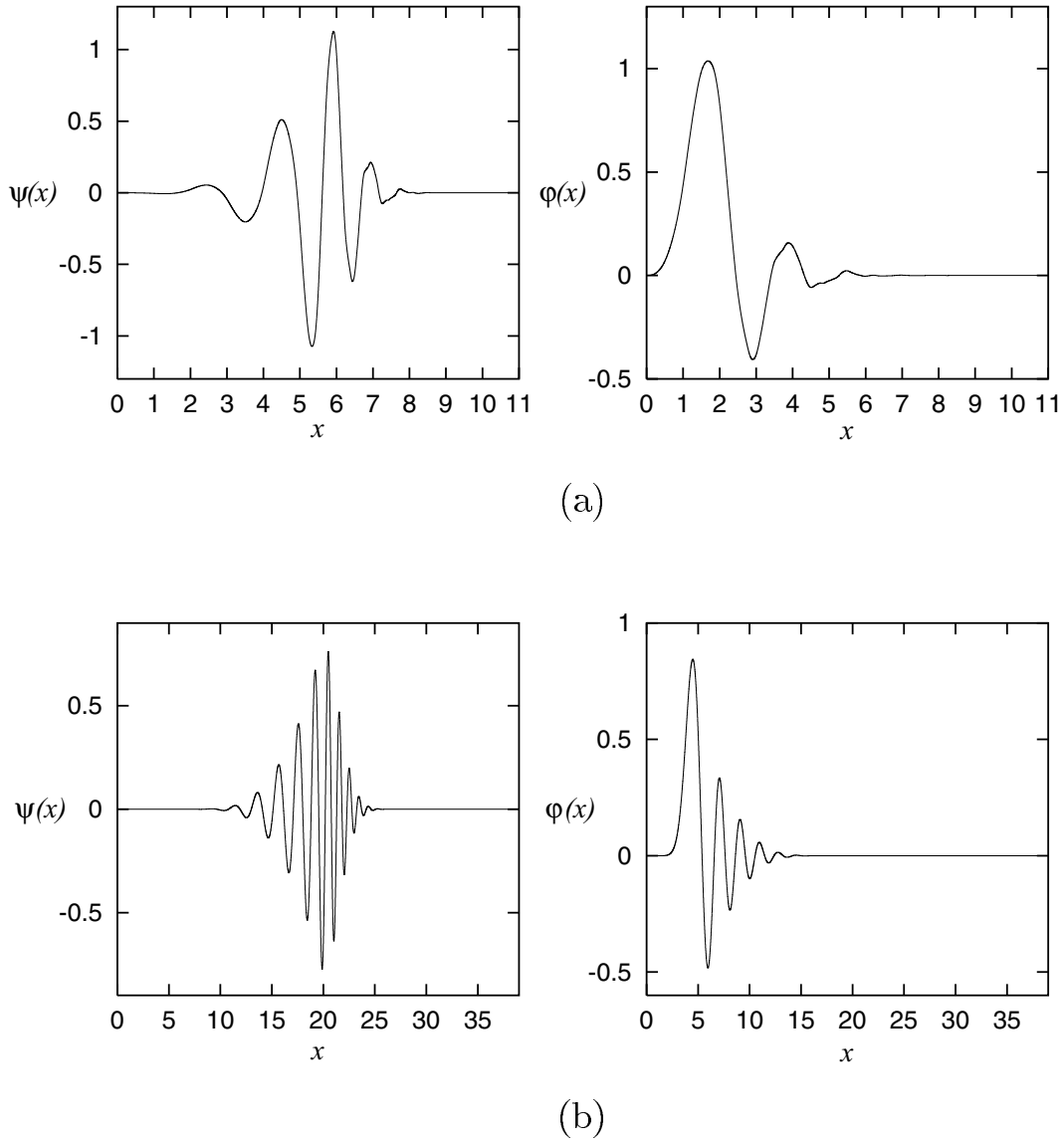

Figure 1. Examples of wavelets $\psi(x)$ and its scaling function $\varphi(x)$ of Daubechies; (a) Daubechies-6 wavelets and (b) Daubechies-20 wavelets.

1.1 Wavelets

After Daubechies (1992) built the foundation of a discrete wavelet transform scheme, a wide range of methods based on wavelets have been adopted in many areas. The ability of the wavelet transform to resolve features at various scales has made wavelet analysis one of most useful techniques in signal processing despite its recent development. Anant & Dowla (1997) compared polarization information across a number of scales in determining *P*-phase arrival time, and used transverse compared to radial amplitude information at different scales in determining *S*-phase. Similar research was done by Tibuleac & Herrin (1999) in a study of *Lg*-phase arrivals using wavelets. Lilly & Park (1995) used multiwavelets to estimate the time-varying spectral density matrix for three-component seismic data. Multiwavelet spectral analysis seeks to minimize the spectral leakage in the spectrum estimates in a similar way to multitaper spectrum analysis. Another approach in signal processing using multiwavelets is to measure the anisotropy at a given area using the relative phase between components to estimate an average particle motion ellipse for the array (Bear *et al.* 1999).

The discrete wavelet transform is based on a multiresolution analysis that decomposes a signal into components of different scales. Decomposition at a given scale is done by sampling using a scaling function $\varphi(x)$, and a companion wavelet function $\psi(x)$. The remaining part of the signal is decomposed using successive higher scales of the scaling function. Fig. 1 shows one pair of scaling function and wavelets (Daubechies-6 and Daubechies-20) used in discrete analysis. An example of signal decomposition onto a wavelet basis is presented in Fig. 2. The chirp signal is decomposed by projecting on a set of subspaces (Q_i, P_j) where Q_i represents the projection on the wavelet subspace with a scale i and P_j the scaling subspace which the orthogonal complement of a wavelet subspace with a scale j.

The wavelet transform is similar to a Fourier transform in the sense that it maps a time function onto 2-D function with a scale a and a translation τ that can be compared to a frequency ω and a time t. When, however, we use the Fourier transform in the time-frequency analysis

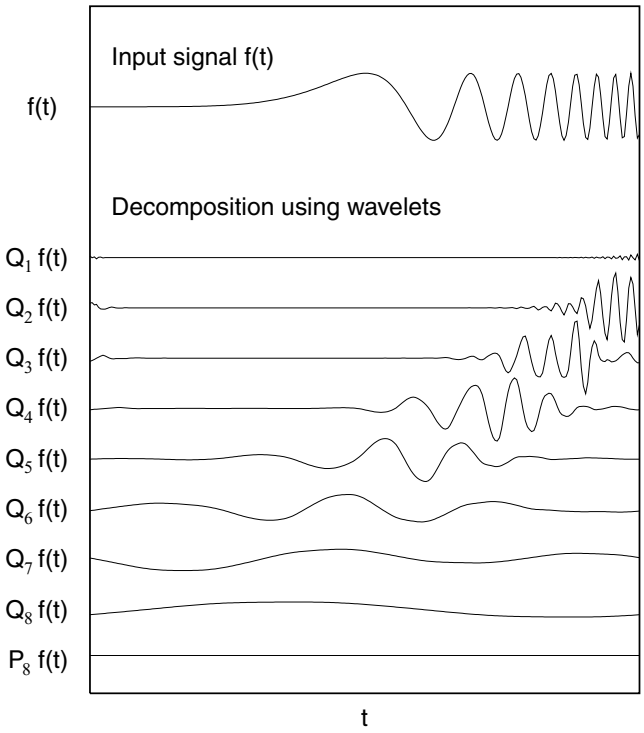

Figure 2. Decomposition of chirp signals using wavelets based on a multiresolution analysis.

of a non-stationary signal in a physical problem, we have two conflicting requirements. The window width T must be long enough to give the desired frequency resolution but must also be short enough so as not to lose the localization in time. A narrow window gives a good time resolution but poor frequency resolution because it has an infinite bandwidth. On the other hand, a wide window gives a good localization in frequency but poor time localization because an impulsive response in frequency does not decay rapidly in time. The sinusoid, basis functions which are used in Fourier transform, are local in frequency but global in time and rely on cancellation to represent discontinuities in time (Chan 1995). Therefore, sinusoids are not efficient in representing functions that have compact support in both time and frequency. However, wavelets are confined in both the frequency and time domains. When we analyse signals at a frequency ω_0 by changing the window width, we can keep the number of cycles of a basis function constant by using wavelets. The confinement characteristics of wavelets allow an extension to the field of numerical analysis. As shown in Fig. 2 the wavelet transform needs only a small number of wavelet subspaces to synthesize a chirp signal, compared to a Fourier transform which would need quite large number of sinusoidal subspaces (basis functions) for such chirp signals.

1.2 Wavelets and PDEs

The application of wavelets in numerical analysis can be generally divided into three streams. One is to simplify the governing partial differential equation (PDE) into a lower order of PDE through a wavelet transform. Lewalle (1998) applied Hermitian wavelets, the derivatives of a Gaussian bell-shaped curve, to a diffusion problem through a canonical transformation and showed a promising development for the numerical prediction of intermittent and nonhomogeneous phenomena. However, this approach has a limitation in the sense that all equations of interest cannot be treated with a certain kind of wavelet. Another approach is the composite use of an FD scheme and an interpolating wavelet transform. Holmström (1999) applied the usual techniques to do all operations in the physical representation and used interpolating wavelets to construct and update the representation. With the help of interpolating wavelets, this scheme achieves the adaptability in domains by imposing a threshold on the wavelet coefficients. Moreover, the scheme is cheap in computation cost compared to other adaptive methods due to the application of FD technique in obtaining the responses of operators. However, this composite scheme suffers from defects of the usual FD scheme as well. The alternative approach is to apply a wavelet transform to the differentiation of a function. A given operator is decomposed into a wavelet basis and then the action of the operator on a function is computed using a wavelet basis which includes the operator effects (Beylkin 1992).

Beylkin (1992) computed the non-standard form (*NS*-form) of several basic operators, such as derivatives and the Hilbert transform, using wavelets. The *NS*-form of operator has an advantage compared with the standard form. We can reduce the effort in applying the operator because *NS*-form of operator is a banded diagonal matrix. Using an *NS*-form of derivative operator and semi-group approach, Beylkin & Keiser (1997) developed an adaptive pseudo-wavelet method for solving non-linear parabolic partial differential equations (PDEs) in one spatial dimension and time.

The adaptive pseudo-wavelet method is based on a semi-group approach, a well-known analytical tool for expressing the solution of PDEs in terms of non-linear integral equations by considering a parabolic PDE as complex of linear and non-linear parts. This wavelet approach combines the desirable features of a FD scheme, spectral methods, and adaptive grid approach. The pseudo-spectral method is similar to the pseudo-wavelet method in the sense that the evolution equation is split into linear and non-linear parts and the contribution of each part is added later. We note that a pseudo-spectral method considers a linear contribution in the Fourier space and a non-linear contribution in the physical space. Therefore, multiple transforms between spaces are needed to cover the full complex contribution.

1.3 Wavelets for wave propagation

Since Beylkin & Keiser's (1997) scheme was developed for parabolic PDEs, it has a limitation in application to other classes of PDEs. So, we need to extend this scheme for elastic wave equations. To apply the scheme for a parabolic PDE to the elastic wave equations, we rewrite the governing equations as a system of first-order PDEs using a displacement-velocity formulation. With this transformation, we can treat elastic wave equations as a simple system of PDEs using wavelets. Also, the system of PDE using displacement-velocity formulation occupies much less memory during computation rather than using a velocity-stress formulation.

The implementation of the traction-free boundary condition at a free surface is one of the important issues in the numerical modelling of elastic wave propagation (e.g. Vidale & Clayton 1986; Ohminato & Chouet 1997). One of the reasons for using a velocity–stress formulation in most numerical methods comes from the direct relation to the boundary condition. Generally, three major approaches have been applied to express the presence of a free-surface. One way is to implement a stress-free boundary condition at the free surface and satisfy the condition explicitly. Gottlieb *et al.* (1982) showed how to use 1-D characteristic variables to enhance the stability of the boundary treatment and Kosloff *et al.* (1990) and Bayliss *et al.* (1986) implemented a traction-free condition by maintaining the magnitude of the outgoing characteristic variables at the boundary. Although this scheme was introduced first by Bayliss *et al.* (1986) for a finite difference method, this approach has proved popular for pseudo-spectral methods (Carcione 1994; Tessmer & Kosloff 1994).

Another approach is to modify the physical parameters (a 'vacuum formalism') and set the elastic wave velocities α, β to zero with the density ρ close to zero above the free surface (Graves 1996). Since, however, a small value of density above a free surface is considered, the time responses often show grid dispersion at a free surface or the Rayleigh waves exhibit rather low frequency content due to progressive energy leakage of incident waves into the vacuum layer. To cure this phenomenon, some researchers have introduced a special treatment of the differentiation of the normal stress term at the free surface (Ohminato & Chouet 1997; Zahradnik 1995; Moczo *et al.* 1997).

An alternative is to use an integrated form of the elastodynamic equations, namely a 'weak (or variational) form'. Faccioli *et al.* (1996) and Komatitsch & Tromp (1999) considered a composite form of equations that includes the governing equation and the boundary conditions at the same time by taking the dot product of each term with an arbitrary test function. The 'weak form' approach has advantages that one can consider the effects at the boundaries implicitly and can overcome the drawbacks in handling non-periodic boundary conditions when using a Fourier method.

In this study, we develop a scheme to express a traction-free condition using displacement variables, not the composite use of velocity and stress variables as in stress-velocity formulation. Also, the condition is implemented in a system of governing equations as an equivalent force term via a semi-group approach. Also, we compare numerical results with analytical solutions in several simple models for validation of the method and show the applicability of the method to complex media. For modelling in media with a surface topography using a wavelet-based method, we refer to Hong & Kennett (2002).

2 PROBLEM FORMULATION

2.1 Semi-group approach

In this section we rewrite the elastic wave equations in the form of a system of first-order partial differential equations (PDEs) and apply a semi-group method by approximating an exponential function of a matrix operator using a Taylor expansion. The detailed procedure is discussed separately for the *SH* wave case and the *P–SV* wave case.

The semi-group approach is used to convert PDEs to non-linear integral equations in time and to estimate the behaviour of the solutions. We consider a time evolution PDE for a variable $g(x, t)$ (Beylkin & Keiser 1997; Belleni-Morante 1979) given by

$$\partial_t g = \mathcal{L}g + \mathcal{N}f(g), \tag{1}$$

where $f(g)$ can be a non-linear function of $g(x, t)$, $\mathcal{L}g$ is a linear part, so $\mathcal{L}$ is a linear operator, $\mathcal{N}f(g)$ is a non-linear part, and so $\mathcal{N}$ is a non-linear operator. The initial condition is

$$g(x, 0) = g_0(x), \qquad 0 \le x \le 1. \tag{2}$$

The solution of the initial value problem for eq. (1) can be represented in the general form

$$g(x, t) = e^{t\mathcal{L}} g_0(x) + \int_0^t e^{(t-\tau)\mathcal{L}} \mathcal{N}f(g(x, \tau))\, d\tau, \tag{3}$$

which can be justified by the method of successive approximations. The solution, eq. (3), verifies the dependence on the initial conditions, and provides for the existence and uniqueness of solutions. Magnitude estimates for $g(x, t)$ can be found by asymptotic analysis.

Beylkin (1992) found a way to represent the operators in eq. (3) in terms of sparse matrices which made it possible to use this semi-group approach as a numerical algorithm to solve a parabolic PDE. By rewriting the elastic wave equations in terms of a first-order PDE system using displacement-velocity scheme, we can apply a semi-group approach to elastic wave equations.

The evolution of eq. (3) in discrete time is investigated by Beylkin *et al.* (1998) and an explicit discretization formula is given by

$$g_{n+1} = e^{\delta t \mathcal{L}} g_n + \delta t \sum_{m=0}^{M-1} \beta_m N_{n-m}, \tag{4}$$

where the coefficient β_m is a function of $\delta t \mathcal{L}$ and controls the order of a quadrature approximation. The g_n is the value of $g(x, t)$ at the discrete times $t_n = t_0 + n\delta t$ for time step δt. N_n represents the non-linear part at time t_n. We note that the separate treatment of linear and non-linear contributions in eqs (3) and (4) makes it possible to implement the time dependent effects (e.g. transient effects, boundary conditions) by considering an additional contribution.

When we consider the elastic wave equation in displacement-velocity form and use a vector form of variables and body force term, we can treat an elastic wave equation using a semi-group approach. In this case, the body-force term is considered as equivalent to a non-linear contribution and the linear operator in eq. (1) is a matrix operator. Also, the traction-free boundary conditions can be introduced as an equivalent force (i.e. additional contribution) in the main equation system. Therefore, we can write the equation as

$$\partial_t \mathbf{U} = \mathbf{L}\mathbf{U} + \mathbf{F}(\mathbf{U}), \tag{5}$$

where $\mathbf{U}$ is a variable vector, $\mathbf{L}$ represents the elastodynamic equation terms through a matrix operator $\mathbf{L}$, and $\mathbf{F}(\mathbf{U})$ represents equivalent force terms (sources and boundary conditions). Thus we can identify a solution of the form eq. (4)

$$\mathbf{U}_{n+1} = e^{\delta t \mathbf{L}} \mathbf{U}_n + \delta t \boldsymbol{\beta}_0 \mathbf{F}_n, \tag{6}$$

in terms of matrix elastic operator. We note that the first order ($M = 1$) of quadrature approximation ($\beta_0 \mathbf{F}_n$) is enough for the consideration of equivalent force contribution since $\mathbf{F}$ is linear in $\mathbf{U}$.

The introduction of the traction-free boundary condition as an equivalent force removes instabilities associated with the free surface. The exponential term in eq. (6) can be approximated via Taylor series (see Sections 2.3 and 2.4).

2.2 Equations

2.2.1 SH waves

When the velocity and density are functions of x and z, the *SH* wave displacement, u_y satisfies the scalar wave equation:

$$\rho \frac{\partial^2 u_y}{\partial t^2} = \frac{\partial}{\partial x}\left(\mu \frac{\partial u_y}{\partial x}\right) + \frac{\partial}{\partial z}\left(\mu \frac{\partial u_y}{\partial z}\right) + f_y, \tag{7}$$

where $\rho(x, z)$ is the density, $\mu(x, z)$ is the shear modulus and $f_y(x, z)$ is the body force at a point (x, z). We can simplify and rewrite the governing eq. (7) introducing a linear operator $\mathcal{L}_y$ as

$$\frac{\partial^2 u_y}{\partial t^2} = \mathcal{L}_y u_y + \frac{f_y}{\rho}, \tag{8}$$

where

$$\mathcal{L}_y = \frac{1}{\rho}\frac{\partial}{\partial x}\left(\mu \frac{\partial}{\partial x}\right) + \frac{1}{\rho}\frac{\partial}{\partial z}\left(\mu \frac{\partial}{\partial z}\right). \tag{9}$$

To apply the semi-group approach to a *SH* wave equation, we rewrite eq. (8) using a relationship between displacement (u_y) and velocity (v_y) of the *SH* wave as a first-order PDE system:

$$\frac{\partial u_y}{\partial t} = v_y, \qquad \frac{\partial v_y}{\partial t} = \mathcal{L}_y u_y + \frac{f_y}{\rho}. \tag{10}$$

We consider the variables, u_y and v_y as components of a vector variable $\mathbf{U}$ and the non-linear term f_y/ρ as a component of a force vector $\mathbf{F}$. The other component in $\mathbf{F}$ is set to zero following eq. (10). The linear operator matrix $\mathbf{L}$ consists of a linear operator $\mathcal{L}_y$, identity term I and zeros (see, eq. (19)).

For stability of the numerical computation around the source, we divide the medium into a source region and the remaining main region. We assume that the source region is an homogeneous and elastic medium. As a force vector $\mathbf{F}$ is considered only in the source region, the procedures for applying the semi-group approach are different for the two regions and will be discussed in Sections 2.3, 2.4.

2.2.2 P–SV waves

The second order partial differential equations describing *P–SV* wave propagation in 2-D media can be written as

$$\frac{\partial^2 u_x}{\partial t^2} = \frac{1}{\rho}\left(\frac{\partial \sigma_{xx}}{\partial x} + \frac{\partial \sigma_{xz}}{\partial z} + f_x\right), \quad \frac{\partial^2 u_z}{\partial t^2} = \frac{1}{\rho}\left(\frac{\partial \sigma_{xz}}{\partial x} + \frac{\partial \sigma_{zz}}{\partial z} + f_z\right), \tag{11}$$

where $(u_x, u_z)_{(m,n)}$ is a displacement vector and $(\sigma_{xx}, \sigma_{xz}, \sigma_{zz})_{(m,n)}$ are stress tensor components at a point (m, n). The stresses $\sigma_{xx}, \sigma_{xz}, \sigma_{zz}$ are given by

$$\sigma_{xx} = (\lambda + 2\mu)\frac{\partial u_x}{\partial x} + \lambda \frac{\partial u_z}{\partial z}, \quad \sigma_{zz} = \lambda \frac{\partial u_x}{\partial x} + (\lambda + 2\mu)\frac{\partial u_z}{\partial z}, \quad \sigma_{xz} = \mu\left(\frac{\partial u_x}{\partial z} + \frac{\partial u_z}{\partial x}\right), \tag{12}$$

where $\lambda(x, z)$ and $\mu(x, z)$ are the Lamé coefficients. The right-hand sides of eq. (11) can be simplified by introducing linear operators $\mathcal{L}_{ij}$ $(i, j = x, z)$:

$$\frac{1}{\rho}\frac{\partial \sigma_{xx}}{\partial x} + \frac{1}{\rho}\frac{\partial \sigma_{xz}}{\partial z} = \mathcal{L}_{xx}u_x + \mathcal{L}_{xz}u_z, \quad \frac{1}{\rho}\frac{\partial \sigma_{xz}}{\partial x} + \frac{1}{\rho}\frac{\partial \sigma_{zz}}{\partial z} = \mathcal{L}_{zx}u_x + \mathcal{L}_{zz}u_z, \tag{13}$$

where the $\mathcal{L}_{ij}$ $(i, j = x, z)$ are given by

$$\begin{aligned} \mathcal{L}_{xx} &= \frac{1}{\rho}\frac{\partial}{\partial x}\left[(\lambda + 2\mu)\frac{\partial}{\partial x}\right] + \frac{1}{\rho}\frac{\partial}{\partial z}\left[\mu\frac{\partial}{\partial z}\right], \quad \mathcal{L}_{xz} = \frac{1}{\rho}\frac{\partial}{\partial x}\left[\lambda\frac{\partial}{\partial z}\right] + \frac{1}{\rho}\frac{\partial}{\partial z}\left[\mu\frac{\partial}{\partial x}\right], \\ \mathcal{L}_{zx} &= \frac{1}{\rho}\frac{\partial}{\partial x}\left[\mu\frac{\partial}{\partial z}\right] + \frac{1}{\rho}\frac{\partial}{\partial z}\left[\lambda\frac{\partial}{\partial x}\right], \quad \mathcal{L}_{zz} = \frac{1}{\rho}\frac{\partial}{\partial x}\left[\mu\frac{\partial}{\partial x}\right] + \frac{1}{\rho}\frac{\partial}{\partial z}\left[(\lambda + 2\mu)\frac{\partial}{\partial z}\right]. \end{aligned} \tag{14}$$

In a similar way to the *SH* wave case, we rewrite the governing equation system (11) as a first-order PDE system by using a displacement-velocity formulation:

$$\begin{aligned} &\frac{\partial u_x}{\partial t} = v_x, \quad \frac{\partial v_x}{\partial t} = \mathcal{L}_{xx}u_x + \mathcal{L}_{xz}u_z + \frac{f_x}{\rho}, \\ &\frac{\partial u_z}{\partial t} = v_z, \quad \frac{\partial v_z}{\partial t} = \mathcal{L}_{zx}u_x + \mathcal{L}_{zz}u_z + \frac{f_z}{\rho}. \end{aligned} \tag{15}$$

Here v_x and v_z are the velocity components in the x and z direction. In *P–SV* wave case, the vector variable $\mathbf{U}$ consists of v_x, v_z, u_x and u_z. Moreover, a force vector $\mathbf{F}$ is composed of the terms $(f_x/\rho, f_z/\rho)$ and zeros. We note that the displacement-velocity formulation implemented in this study can reduce the memory requirements during computation by about 30 per cent compared to a usual velocity-stress formulation.

The spatial derivatives ∂_k $(k = x, z)$ in the *SH* and *P–SV* wave equations are treated with the use of wavelet transform and these differentiated displacement or velocity fields can be considered independently. Therefore, it is possible to treat the elastic wave equations through a first-order PDE system via the introduction of linear operators $\mathcal{L}_{i,j}$ $(i, j = x, z)$ or $\mathcal{L}_y$. Wavelets can achieve any order of differentiation of a function by considering a derivative operator in wavelet bases. So, we have an advantage that we can obtain a differentiated function with one application of operator in wavelet bases regardless of the order of derivative. The simplicity in the differentiation procedure is similar to a Fourier transform. But, wavelets are more efficient in the sense that we can predict the phenomenon more easily because of their application in the time domain. The differentiation scheme in the 2-D domain is discussed in Section 3.1.

2.3 Source region

If we use heterogeneous-media scheme for wavelets directly in the source region, we often have unstable results due to multiple differentiation of the delta function representing a point source. Therefore, we assume that the source region is homogeneous and apply an homogeneous-medium scheme around the source region. In this case, the linear operators $\mathcal{L}_{ij}$ $(i, j = x, z)$ in eq. (14) can be rewritten by

$$\mathcal{L}^h_{xx} = \frac{\lambda + 2\mu}{\rho}\frac{\partial^2}{\partial x^2} + \frac{\mu}{\rho}\frac{\partial^2}{\partial z^2}, \quad \mathcal{L}^h_{xz} = \mathcal{L}^h_{zx} = \frac{\lambda + \mu}{\rho}\frac{\partial^2}{\partial x \partial z}, \quad \mathcal{L}^h_{zz} = \frac{\mu}{\rho}\frac{\partial^2}{\partial x^2} + \frac{\lambda + 2\mu}{\rho}\frac{\partial^2}{\partial z^2}, \tag{16}$$

and $\mathcal{L}_y$ in (9) is simplified to

$$\mathcal{L}^h_y = \frac{\mu}{\rho}\frac{\partial^2}{\partial x^2} + \frac{\mu}{\rho}\frac{\partial^2}{\partial z^2}. \tag{17}$$

The superscript h is added to the linear operators for the homogeneous case to distinguish them from the more general ones. Eqs (10) and (15) can be expressed in first order differential equation form as

$$\partial_t \mathbf{U} = \mathbf{L}_h \mathbf{U} + \mathbf{F}, \tag{18}$$

where $\mathbf{L}_h$ is a matrix operator in an homogeneous medium and $\mathbf{F}$ is a force term vector. For the *SH* wave case, $\mathbf{U}$, $\mathbf{L}_h$, $\mathbf{F}$ are given by

$$\mathbf{U} = \begin{pmatrix} u_y \\ v_y \end{pmatrix}, \quad \mathbf{L}_h = \begin{pmatrix} 0 & I \\ \mathcal{L}_y^h & 0 \end{pmatrix}, \quad \mathbf{F} = \frac{1}{\rho}\begin{pmatrix} 0 \\ f_y \end{pmatrix}, \tag{19}$$

and for the *P–SV* wave case,

$$\mathbf{U} = \begin{pmatrix} u_x \\ v_x \\ u_z \\ v_z \end{pmatrix}, \quad \mathbf{L}_h = \begin{pmatrix} 0 & I & 0 & 0 \\ \mathcal{L}_{xx}^h & 0 & \mathcal{L}_{xz}^h & 0 \\ 0 & 0 & 0 & I \\ \mathcal{L}_{zx}^h & 0 & \mathcal{L}_{zz}^h & 0 \end{pmatrix}, \quad \mathbf{F} = \frac{1}{\rho}\begin{pmatrix} 0 \\ f_x \\ 0 \\ f_z \end{pmatrix}, \tag{20}$$

where (v_x, v_z) is a velocity vector. Following eq. (6), we can write an explicit discrete time solution as

$$\mathbf{U}_{n+1} = e^{\delta t \mathbf{L}_h}\mathbf{U}_n + \delta t \boldsymbol{\beta}_0 \mathbf{F}_n, \tag{21}$$

where $\mathbf{F}_n$ is a force vector at a discretized time t_n and $\boldsymbol{\beta}_0$ is given by $(e^{\delta t \mathbf{L}_h} - \mathbf{I})\ (\delta t \mathbf{L}_h)^{-1}$ (see Beylkin *et al.* 1998). $e^{\delta t \mathbf{L}_h}$ and $\boldsymbol{\beta}_0$ can be approximated by a Taylor expansion:

$$e^{\delta t \mathbf{L}_h} = \mathbf{I} + \delta t \mathbf{L}_h + \frac{1}{2}\delta t^2 \mathbf{L}_h^2 + \frac{1}{6}\delta t^3 \mathbf{L}_h^3 + \cdots, \quad \boldsymbol{\beta}_0 = \mathbf{I} + \frac{1}{2}\delta t \mathbf{L}_h + \frac{1}{6}\delta t^2 \mathbf{L}_h^2 + \frac{1}{24}\delta t^3 \mathbf{L}_h^3 + \cdots. \tag{22}$$

The resultant forms of $e^{\delta t \mathbf{L}_h}$ and $\boldsymbol{\beta}_0$ are given in Appendix A.

2.4 The main region

We can simulate the remainder of the medium by considering the responses at the source region via boundary conditions. As the body force only needs to be considered in the source region and its effect is transmitted to the main region via boundary conditions, we can omit the source term f_i $(i = x, y, z)$ in the governing eqs (7) and (11). Therefore, the first-order differential equation system can be rewritten as

$$\partial_t \mathbf{U} = \mathbf{L}_h \mathbf{U}, \tag{23}$$

where $\mathbf{L}$ is a 4-by-4 matrix operator in a *P–SV* wave problem and is 2-by-2 for a *SH* wave (Appendix B). The linear operators $\mathcal{L}_y$, $\mathcal{L}_{ij}$ $(i, j = x, z)$, the components of $\mathbf{L}$, are given in eqs (9) and (14). Using a semi-group approach and the discrete representation (4), eq. (23) can be discretized as

$$\mathbf{U}_{n+1} = e^{\delta t \mathbf{L}}\mathbf{U}_n, \tag{24}$$

where $e^{\delta t \mathbf{L}}$ is evaluated using a Taylor expansion in (22), the resultant matrix is given in Appendix B.

2.5 Formulation including absorbing boundary conditions

Following Cerjan *et al.* (1985), a filtering scheme forcing the decay of wave amplitudes by multiplying an attenuation factor, has been used in handling artificial boundaries (Sochacki *et al.* 1987; Kosloff & Kosloff 1986). This filtering scheme is also effective for the case when the events impinge on the boundaries at shallow angles, unlike the paraxial approximation scheme (Clayton & Engquist 1977; Stacey 1988; Mahrer 1990). To achieve a consistent treatment of the application of absorbing boundary condition and for a quantitative analysis, the attenuation factors have come to be considered as attenuation terms included in the elastic wave equation (Kosloff & Kosloff 1986; Sochacki *et al.* 1987).

When we consider the *P–SV* wave equations including attenuation factors (Q_x, Q_z) in the main region scheme, the equations in (11) can be rewritten as (Sochacki *et al.* 1987)

$$\begin{aligned} \frac{\partial^2 u_x}{\partial t^2} + 2Q_x \frac{\partial u_x}{\partial t} &= \frac{1}{\rho}\left(\frac{\partial \sigma_{xx}}{\partial x} + \frac{\partial \sigma_{xz}}{\partial z}\right), \\ \frac{\partial^2 u_z}{\partial t^2} + 2Q_z \frac{\partial u_z}{\partial t} &= \frac{1}{\rho}\left(\frac{\partial \sigma_{xz}}{\partial x} + \frac{\partial \sigma_{zz}}{\partial z}\right), \end{aligned} \tag{25}$$

and the *SH* wave equation with $Q_y(x, z)$ is,

$$\frac{\partial^2 u_y}{\partial t^2} + 2Q_y \frac{\partial u_y}{\partial t} = \frac{1}{\rho}\frac{\partial}{\partial x}\left(\mu \frac{\partial u_y}{\partial x}\right) + \frac{1}{\rho}\frac{\partial}{\partial z}\left(\mu \frac{\partial u_y}{\partial z}\right). \tag{26}$$

In this section, we describe the application to the *P–SV* wave case for the main region. When we consider the *P–SV* wave equations in (25) in the form of the first order differential equation system in (23), the matrix operator $\mathbf{L}_q$ can be written as

$$\mathbf{L}_q = \begin{pmatrix} 0 & I & 0 & 0 \\ \mathcal{L}_{xx} & -2Q_x & \mathcal{L}_{xz} & 0 \\ 0 & 0 & 0 & I \\ \mathcal{L}_{zx} & 0 & \mathcal{L}_{zz} & -2Q_z \end{pmatrix}. \tag{27}$$

Following (24) and evaluating $e^{\delta t \mathbf{L}_q}$ by a Taylor expansion, we discretize the first order differential equation system. When we neglect the product terms $\mathcal{L}_{ij}\mathcal{L}_{kl}$, the discretized solution of (25) including an intrinsic attenuation term is given by

$$\begin{pmatrix} u_x^{n+1} \\ v_x^{n+1} \\ u_z^{n+1} \\ v_z^{n+1} \end{pmatrix} = \begin{pmatrix} B_{11} & B_{12} & B_{13} & B_{14} \\ B_{21} & B_{22} & B_{23} & B_{24} \\ B_{31} & B_{32} & B_{33} & B_{34} \\ B_{41} & B_{42} & B_{43} & B_{44} \end{pmatrix} \begin{pmatrix} u_x^{n} \\ v_x^{n} \\ u_z^{n} \\ v_z^{n} \end{pmatrix}, \tag{28}$$

where the components B_{ij} $(i, j = 1, 2, 3, 4)$ are:

$$\begin{aligned}
B_{11} &= I + \frac{\delta t^2}{2}\mathcal{L}_{xx} - \frac{\delta t^3}{3}Q_x\mathcal{L}_{xx}, \\
B_{12} &= \delta t I - \delta t^2 Q_x + \frac{2}{3}\delta t^3 Q_x^2 + \frac{\delta t^3}{6}\mathcal{L}_{xx}, \\
B_{13} &= \frac{\delta t^2}{2}\mathcal{L}_{xz} - \frac{\delta t^3}{3}Q_x\mathcal{L}_{xz}, \qquad B_{14} = \frac{\delta t^3}{6}\mathcal{L}_{xz}, \\
B_{21} &= \delta t\mathcal{L}_{xx} - \delta t^2 Q_x\mathcal{L}_{xx}, \\
B_{22} &= I - 2\delta t Q_x + 2\delta t^2 Q_x^2 - \frac{4}{3}\delta t^3 Q_x^3 + \frac{\delta t^2}{2}\mathcal{L}_{xx} - \frac{2}{3}\delta t^3 Q_x\mathcal{L}_{xx}, \\
B_{23} &= \delta t\mathcal{L}_{xz} - \delta t^2 Q_x\mathcal{L}_{xz}, \qquad B_{24} = \frac{\delta t^2}{2}\mathcal{L}_{xz} - \frac{\delta t^3}{3}(Q_x + Q_z)\mathcal{L}_{xz}, \\
B_{31} &= \frac{\delta t^2}{2}\mathcal{L}_{zx} - \frac{\delta t^3}{3}Q_z\mathcal{L}_{zx}, \qquad B_{32} = \frac{\delta t^3}{6}\mathcal{L}_{zx}, \\
B_{33} &= I + \frac{\delta t^2}{2}\mathcal{L}_{zz} - \frac{\delta t^3}{3}Q_z\mathcal{L}_{zz}, \\
B_{34} &= \delta t I - \delta t^2 Q_z + \frac{2}{3}\delta t^3 Q_z^2 + \frac{\delta t^3}{6}\mathcal{L}_{zz}, \qquad B_{41} = \delta t\mathcal{L}_{zx} - \delta t^2 Q_z\mathcal{L}_{zx}, \\
B_{42} &= \frac{\delta t^2}{2}\mathcal{L}_{zx} - \frac{\delta t^3}{3}(Q_x + Q_z)\mathcal{L}_{zx}, \qquad B_{43} = \delta t\mathcal{L}_{zz} - \delta t^2 Q_z\mathcal{L}_{zz}, \\
B_{44} &= I - 2\delta t Q_z + 2\delta t^2 Q_z^2 - \frac{4}{3}\delta t^3 Q_z^3 + \frac{\delta t^2}{2}\mathcal{L}_{zz} - \frac{2}{3}\delta t^3 Q_z\mathcal{L}_{zz}.
\end{aligned} \tag{29}$$

Eq. (28) is introduced in the main region and satisfies the absorbing boundary condition implicitly. However in the source region we do not include attenuation factors because we consider only a few grid points around the source.

2.6 Source

2.6.1 SH waves

We apply a point source for all *SH* wave propagation problems in this study and assume that the point source generates only pure shear waves. The body force for *SH* wave case is given by

$$f_y(x, z, t) = \delta(x - x_s)\delta(z - z_s)h(t), \tag{30}$$

where $h(t)$ is a source time function and (x_s, z_s) is a source position. Following Alford *et al.* (1974), the time history of an impulsive excitation $h(t)$ has been taken as

$$h(t) = C_s(t - t_0)e^{-w(t-t_0)^2}, \tag{31}$$

where C_s is a constant, t_0 is a shifted time value and w controls the wavelength content of the excitation. In this study, we set $t_0 = 0.2$ s and $w = 200$.

2.6.2 P–SV waves

We introduce two kinds of sources: a vertically directed force and an explosive point source. The vertically directed force is used in Lamb's (1904) problem for the comparison between numerical results and analytic solutions, and in the case of a velocity model with a linear

gradient. An explosive point source is implemented in the tests of absorbing boundary conditions for the *P–SV* wave case and in a two layered heterogeneous model, because this source generates only compressional waves and simplifies the wavefields. To design a vertically directional force, we set f_x to zero and apply the point source described in *SH* wave case to f_z. The design of an explosive point source is possible by the introduction of an equivalent body force system using a moment tensor $M_{ij}(t)$ which is given by (e.g. Kennett 1988)

$$M_{ij}(t) = M_{ij}h(t), \tag{32}$$

where $h(t)$ is the source time function in (31). The explosive point source can be simulated with isotropic dipole forces on each axis:

$$M_{xx}(t) = M_{zz}(t) = M_0h(t), \quad M_{xz}(t) = M_{zx}(t) = 0, \tag{33}$$

where M_0 is a seismic moment. Therefore, the body forces f_x and f_z for an explosive source can be described by (Ben-Menahem & Singh 1981)

$$f_x(x, z, t) = -M_0h(t)\frac{\partial}{\partial x}\delta(x - x_s)\delta(z - z_s), \quad f_z(x, z, t) = -M_0h(t)\delta(x - x_s)\frac{\partial}{\partial z}\delta(z - z_s), \tag{34}$$

where (x_s, z_s) is the source position.

Unlike a FD scheme which needs a generalized moment tensor with first-order accuracy in representing source effects for stable computation (Frankel 1993; Graves 1996), a wavelet-based method can obtain an equivalent body force system (34) by differentiating the delta function directly with sustenance of numerical accuracy in a main procedure.

2.7 Initial conditions

The media are supposed to be in equilibrium at time $t = 0$, i.e. the displacement fields (u_x, u_z) and velocity fields (v_x, v_z) are set to zero everywhere in the media.

2.8 Free surface boundary condition

The accurate representation of the free surface boundary condition is one of the most important problems in numerical seismology. The condition at the Earth's surface is the requirement of zero traction. Therefore, for a flat free surface normal to the z-axis the condition is that

$$[\sigma_{iz}]_{z=0} = 0, \qquad i = x, y, z. \tag{35}$$

Even in a velocity-stress formulation the traction-free condition cannot be satisfied directly because of the influence of the unconstrained variables (e.g. σ_{xx}, v_x, v_z). Gottlieb *et al.* (1982) and Thompson (1990) have investigated stable and accurate implementation of the boundary conditions for hyperbolic systems of PDEs.

In this study, we introduce a scheme for implementation of a traction-free condition in a displacement-velocity based system exactly and stably. We consider the traction-free boundary condition independently from the main computational procedure by considering the boundary condition with equivalent force terms through a semi-group approach. In other words, we introduce the boundary condition to governing equations using equivalent terms and treat those effects with semi-group approach. We expect this scheme can be an effective method for implementation of various boundary conditions which can be existed simultaneously or difficult to implement at the time in media by considering the boundary conditions separately with additional equivalent force terms.

Since a wavelet-based method is a non-grid based scheme for a spatial differentiation, it is necessary to implement the boundary conditions for a band of reference points (Hong & Kennett 2002). Therefore, we set μ and λ to be zero above a free surface using the vacuum formalism to prevent any spurious wave propagation into the vacuum layer and to impose the boundary condition at the free surface.

2.8.1 SH waves

Since we set *SH* waves to be polarized along the y-axis in a Cartesian co-ordinate, $u_x = u_z = 0$. Therefore, $\sigma_{xz} = \sigma_{zz} = 0$ intrinsically and only σ_{yz} has to satisfy the condition at the free surface. Since σ_{yz} vanishes at a free surface, we can include this condition in the governing equation system by writing

$$\frac{\partial}{\partial t}\begin{pmatrix} u_y \\ v_y \end{pmatrix} = \begin{pmatrix} 0 & I \\ \mathcal{L}_y & 0 \end{pmatrix}\begin{pmatrix} u_y \\ v_y \end{pmatrix} + \frac{1}{\rho}\begin{pmatrix} 0 \\ f_y - \partial_z\left(\sigma_{yz}^F\right) \end{pmatrix}, \tag{36}$$

where $\delta(z)$ is a Dirac delta and σ_{yz}^F is a free-surface tangential stress vector which is set to be zero except a free surface:

$$\sigma_{yz}^F = \delta(z)\left(\mu\frac{\partial u_y}{\partial z}\right). \tag{37}$$

As the force term f_y/ρ is considered at the source region scheme, only the boundary effect term is considered in the main region scheme. The procedure for handling the equivalent force term in the main-region scheme follows the approach used for the source region.

2.8.2 P–SV waves

From (35), the free surface boundary conditions for *P–SV* wave case in 2-D space require normal and tangential stresses to vanish ($\sigma_{zz} = \sigma_{xz} = 0$) at the flat free surface ($z = 0$). Before we consider the boundary conditions at a free surface, we modify the other stress term σ_{xx} by imposing the traction-free condition. We rewrite the spatial derivative term in z direction in σ_{xx} using $\sigma_{zz} = 0$ and obtain an expression for σ_{xx} in terms of just the horizontal derivative of u_x:

$$\sigma_{xx}|_{z=0} = \frac{4\mu(\lambda+\mu)}{(\lambda+2\mu)}\frac{\partial u_x}{\partial x}. \tag{38}$$

We note that expression (38) is the same as that expressed by decomposing the wavefield into one-way modes for the boundary conditions (namely '1-D analysis') in Carcione (1994). Using (35) and (38), we can express the governing equations in (11) including the traction-free condition by

$$\begin{aligned}
\frac{\partial^2 u_x}{\partial t^2} &= \frac{1}{\rho}\left\{\frac{\partial}{\partial x}\left(\sigma_{xx} - \sigma_{xx}^F + \sigma_{xx}^M\right) + \frac{\partial}{\partial z}\left(\sigma_{xz} - \sigma_{xz}^F\right) + f_x\right\},\\
\frac{\partial^2 u_z}{\partial t^2} &= \frac{1}{\rho}\left\{\frac{\partial}{\partial x}\left(\sigma_{xz} - \sigma_{xz}^F\right) + \frac{\partial}{\partial z}\left(\sigma_{zz} - \sigma_{zz}^F\right) + f_z\right\},
\end{aligned} \tag{39}$$

where,

$$\begin{aligned}
\sigma_{ij}^F &= \delta(z)\sigma_{ij}, \quad i, j = x, z,\\
\sigma_{xx}^M &= \delta(z)\left\{\frac{4\mu(\lambda+\mu)}{\lambda+2\mu}\frac{\partial u_x}{\partial x}\right\}.
\end{aligned} \tag{40}$$

If we treat the equivalent force terms added for the traction-free boundary condition in (39) as the non-linear terms, we can rewrite a *P–SV* governing equation system with implicit absorbing boundary conditions (25) as

$$\frac{\partial}{\partial t}\begin{pmatrix} u_x \\ v_x \\ u_z \\ v_z \end{pmatrix} = \begin{pmatrix} 0 & I & 0 & 0 \\ \mathcal{L}_{xx} & -2Q_x & \mathcal{L}_{xz} & 0 \\ 0 & 0 & 0 & I \\ \mathcal{L}_{zx} & 0 & \mathcal{L}_{zz} & -2Q_z \end{pmatrix}\begin{pmatrix} u_x \\ v_x \\ u_z \\ v_z \end{pmatrix} + \frac{1}{\rho}\begin{pmatrix} 0 \\ f_x - \partial_x\left(\sigma_{xx}^F\right) - \partial_z\left(\sigma_{xz}^F\right) + \partial_x\left(\sigma_{xx}^M\right) \\ 0 \\ f_z - \partial_x\left(\sigma_{xz}^F\right) - \partial_z\left(\sigma_{zz}^F\right) \end{pmatrix}. \tag{41}$$

As in the *SH* wave case, we apply the scheme in the main-region computation.

3 NUMERICAL ANALYSIS

3.1 Calculation of linear operators in 2-D

Following the scheme developed by Beylkin & Keiser (1997), we apply a wavelet transform to obtain the effect of the linear operators on the displacement or velocity fields ($\mathcal{L}u^n$ or $\mathcal{L}v^n$) at a discretized time t_n. Each $\mathcal{L}_{ij}$ $(i, j = x, z)$ and $\mathcal{L}_y$ are composed of two spatial derivative terms of the form $\partial_i(a\partial_j g^n)$ $(i, j = x, z)$ where g^n represents the displacement or velocity fields at time t_n and a is a function of λ and μ. First, we differentiate g^n in the j direction for a whole domain. The first order differentiated 2-D fields multiplied by a are used as input fields for the other spatial differentiation, ∂_i.

We use the Daubechies-20 wavelets (Fig. 1(b)) which have 20 vanishing moments and 40 wavelet coefficients. The larger the number of vanishing moments of the wavelets, the better the resolution of the sudden variations of physical parameters in heterogeneous media. We follow the differentiation scheme in Beylkin (1992). From (16) and (17), we need not only the first-order differentiation operator, but also the second order differentiation operator (∂_i^2, $i = x, z$) for the computation in a source region. The coefficients (r_l^1, r_l^2 where $-38 \le l \le 38$) of the non-standard form of first- and second-order spatial differentiation operator (∂_i, ∂_i^2, $i = x, z$) based on Daubechies-20 wavelets, can be computed following (4.3) and (4.4) in Beylkin (1992). The coefficients r_l^1 for Daubechies-20 wavelets are given in Appendix C.

The inherent assumption of differentiation of 2-D displacement or velocity fields using wavelets is that vertical and horizontal dimension of domain are same as each other regardless of numbers of reference points included for each direction. This characteristic makes it possible to use different sizes of grid step in each direction. When we differentiate a velocity or a displacement fields horizontally in a domain with twice the horizontal length compared to vertical length, we can stay apace with elastic wave propagation in every direction by multiplying by an additional factor of $1/2$ for every horizontal differentiation of the fields.

In this section, we discussed treatment of the linear operators and associated features in the wavelet-based method without mathematical consideration of operators on wavelet bases as it is out of scope of the paper. We refer to Beylkin & Keiser (1997) for the details of the projection of operators on to the wavelet bases (see also Hong & Kennett 2002).

3.2 Numerical aspects

The stability condition is independent of the S wave velocity or of the Poisson's ratio ν. The usual stability condition for a finite difference method in 2-D case is given by (Virieux 1986)

$$\alpha \delta t \sqrt{\frac{1}{\delta x^2} + \frac{1}{\delta z^2}} < 1, \tag{42}$$

where δt is the time step, δx is the grid step for the x-axis, δz for the z-axis and we set δx to be equal to δz. We apply an empirical stability condition based on a finite difference method in this study:

$$C_w \alpha_{\max} \frac{\delta t}{\delta z} < 1, \tag{43}$$

where C_w is a constant and $\alpha_{\max}$ is the highest wave velocity of the domain. The constant C_w is controlled by the extent of order of terms considered in the Taylor expansion for the discrete time solutions in eq. (22). In this study, we consider up to third orders of terms in the Taylor expansion and the numerical results are stable when $C_w = 10$.

The minimum number of grid points per smallest wavelength varies with a type of wavelets which are used. Generally, for Daubechies wavelets, the number of grid points needed per wavelength can be reduced by a half when twice higher-order wavelets (e.g. Daubechies-6: Daubechies-12) are implemented. For example, Daubechies-3 wavelets need about 32 grid points per wavelength for numerically stable computation, Daubechies-6 needs 16 points, Daubechies-9 needs 8 points and Daubechies-20 needs 3 points. However, this relationship can not be carried indefinitely for much higher wavelets because it is difficult to compute higher wavelet coefficients using any known numerical scheme (Shensa 1992; Strang & Nguyen 1996) and the resultant coefficients are unstable with the increase of the number of vanishing moments of wavelets. Moreover, the magnitude of coefficients can be smaller than round-off error in the numerical modelling and their calculation may require excessive numerical precision. In this study, we apply Daubechies-20 wavelets.

For numerical simulation of *P–SV* wave propagation in 2-D media with 128-by-128 grid points, the memory required is of the order of 10 Megabytes. The CPU time for simulation over 403 time steps (corresponding to 1.0 s in a time response) is of the order of 110 min on a Compaq XP1000, where the time step (δt) is 0.00248 s when maximum compressional wave velocity (α) in a domain is 3.15 km s^{-1}.

4 ELASTIC WAVE PROPAGATION

4.1 Test of absorbing boundary conditions

To test the efficiency of the attenuation terms in eqs (25) and (26) for the waves approaching the artificial boundaries, we check the absorption of the displacement fields at the artificial boundaries in a 2-D homogeneous medium (Fig. 3) with compressional velocity 3.15 km s^{-1}, shear velocity 1.8 km s^{-1} and density 2.2 g cm^{-3}.

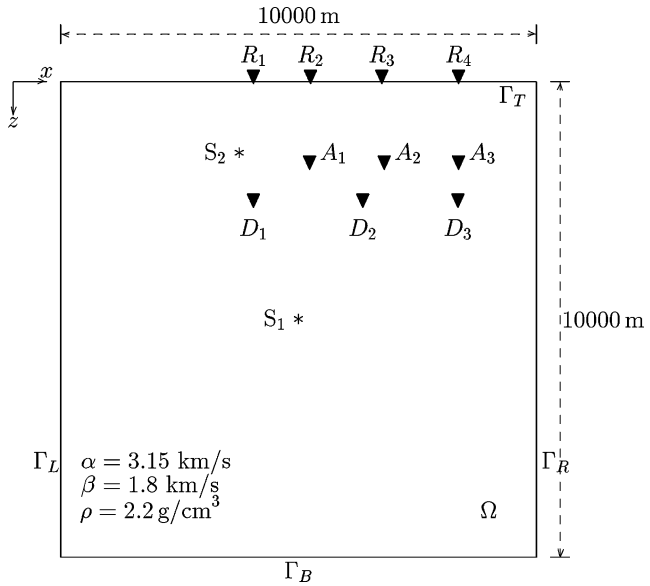

Figure 3. Description of 2-D homogeneous elastic media used for a test of absorbing boundaries and for a modelling of elastic wave propagation in the presence of a free surface (Lamb's problem). Source S_1 is a source position for a test of absorbing boundaries and S_2 for a Lamb's problem. Also, receivers R_j, A_j and D_j are placed horizontally at each depth ($h = 0$, 1719 and 2500 m) in the medium to obtain time responses for numerical comparisons.

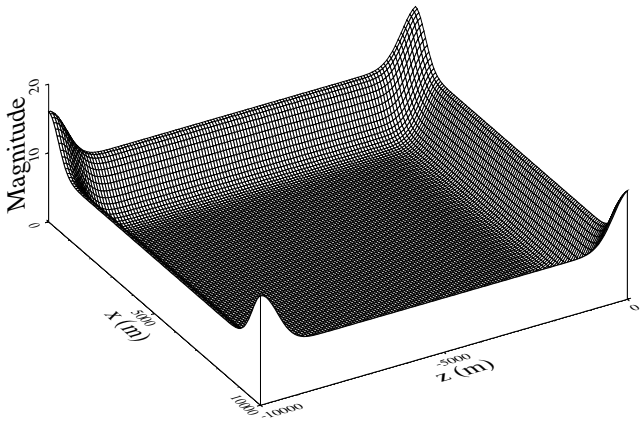

Figure 4. Distribution of attenuation factors (Q_j, $j = x, y, z$) on a 2-D medium with four absorbing boundaries when $\mathcal{A}_x = \mathcal{A}_z = 8$ and $\mathcal{B}_x = \mathcal{B}_z = -0.015$ in (44).

The attenuation factors (Q_x & Q_z for *P–SV* wave case, Q_y for *SH* wave case) are designed following conditions suggested by Sochacki *et al.* (1987) so that these attenuation factors are bounded, twice continuously differentiable and their derivatives are sufficiently smooth on a domain. In this study, we distribute attenuation factors on a domain by

$$Q_j(i_x, i_z) = \mathcal{A}_x\left[e^{\mathcal{B}_x i_x^2} + e^{\mathcal{B}_x (i_x - N_x)^2}\right] + \mathcal{A}_z\left[e^{\mathcal{B}_z i_z^2} + e^{\mathcal{B}_z (i_z - N_z)^2}\right], \qquad j = x, y, z, \qquad i_x = 1, 2, \ldots, N_x, \qquad i_z = 1, 2, \ldots, N_z, \tag{44}$$

where $\mathcal{A}_k$ and $\mathcal{B}_k$ ($k = x, z$) are constants determined by considering the wave speeds in media, N_x is the number of grid points in the x direction, N_z the total number of grid points in the z direction and (i_x, i_z) is a discretized grid position. $\mathcal{A}_j$ controls the magnitude of attenuation and $\mathcal{B}_j$ modulates the width of the attenuation area. In this experiment, we set $\mathcal{A}_j$ ($j = x, z$) is to be 8 and $\mathcal{B}_j$ to -0.015 (Fig. 4).

We apply a point source in the *SH* wave case and compressional and vertically-directed point forces for the *P–SV* wave case. Fig. 5 shows the absorption of displacement fields at four absorbing boundaries with time. The direct phases are absorbed effectively at the boundaries, spurious waves reflected from the boundaries are weak enough not to spoil the wavefields. To provide a quantitative check on the time responses in the presence of absorbing boundaries, we consider three receivers placed horizontally at the 21st gridpoint below the top absorbing boundary (A_j, $j = 1, 2, 3$ in Fig. 3) where free surface receivers are placed in later experiments (Fig. 6). The major spurious waves are indicated by arrows to compare with the main phases (*P*, *S*). We note that generally *P* phases are absorbed well at the boundaries, but small amounts of *S* phases are reflected from the absorbing boundaries. Spurious waves develop following the *S* waves due to the differences in wavelengths compared to the gradients in the attenuation factors. As shown in A and B in Fig. 6, this effect is more marked at four corners of domain where the gradients in the attenuation factors are augmented (see Fig. 4).

4.2 Test of accuracy in unbounded media

In Figs 7 and 8 we consider a numerical test of wave excitation by a delta function source using the wavelet approach with comparison with analytic solutions (Pilant 1979) for four receivers (R_j, $j = 1, \ldots, 4$ in Fig. 7) at 5938 to 8397 m from the source (Fig. 8).
Because the wavelet transform can provide a full description of the effects of a delta function, we get an excellent representation of the wavefield excited by a vertically-directed force at each location. The slight discrepancies at later times come from the absorbing boundary conditions. We also note that the high frequency waves before *S* waves (A in Fig. 8, B in Fig. 10) are related to the fact that the differentiation of delta function (in a source region) using wavelets with a limited band of frequency produces small amplitude high frequency waves before and after the exact solutions. This phenomenon also can be found in a Fourier method (Kosloff *et al.* 1984; Tal-Ezer *et al.* 1987).

4.3 Homogeneous media with a free surface

4.3.1 SH waves

Since the *SH* wave equation is relatively simple and does not generate additional phases at the free surface, a *SH* wave front can be simulated easily by introducing virtual image sources (Virieux 1984). But, in this study, we introduce a way of implementing a traction-free condition in *SH* wave equation without use of a virtual image scheme. We introduce a point source just beneath a free surface and then model the response of *SH* wave.

To treat a top boundary in the media as a free surface, we modify the attenuation factors (Q_j, $j = x, y, z$) in eqs (25) and (26) so as not to absorb the waves approaching to a free surface by a vertical shift in the distribution of the attenuation factors:

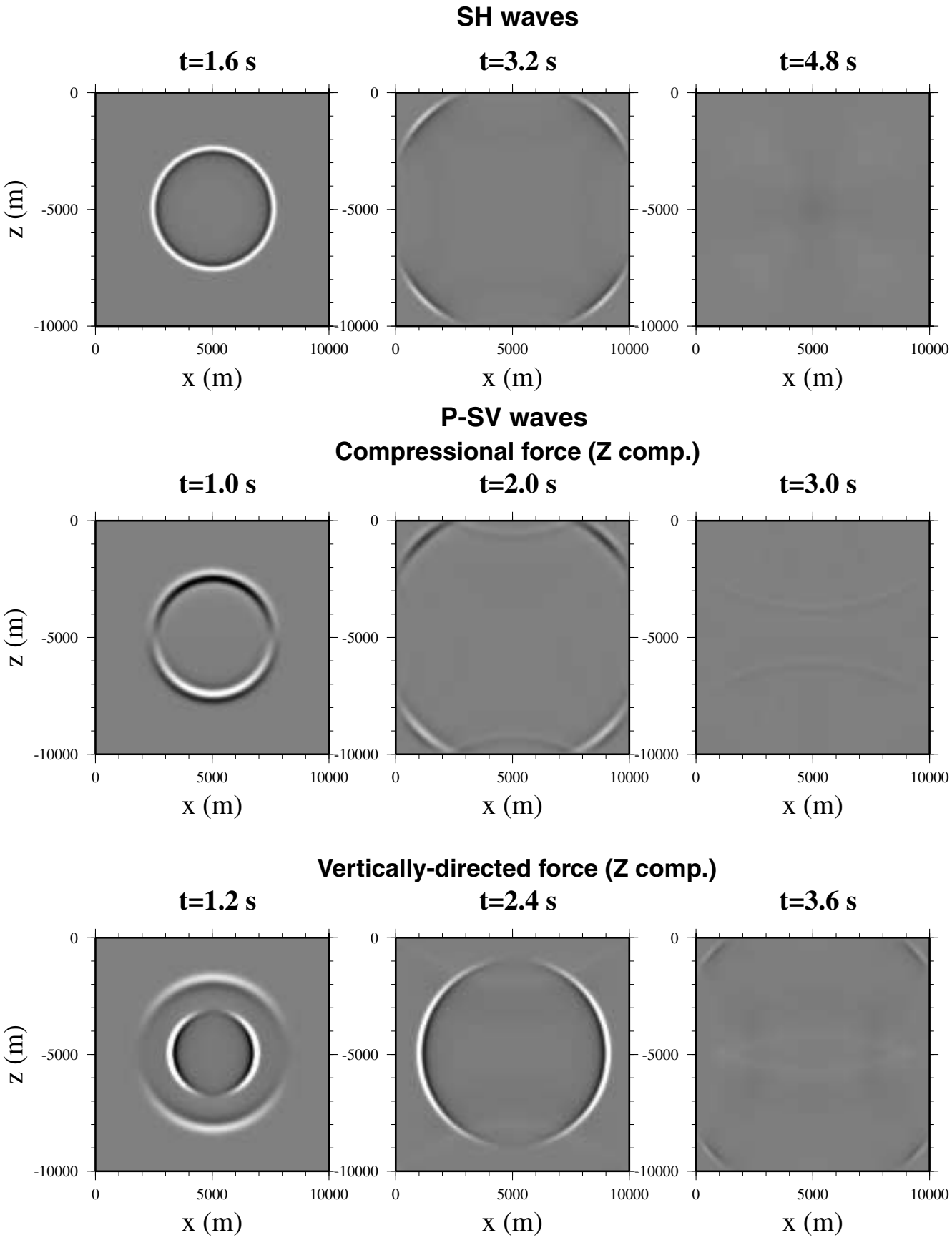

Figure 5. Successive snapshots of *SH* and *P–SV* wave propagation in an homogeneous elastic medium where four artificial boundaries are treated by the absorbing boundary condition. For a test of *P–SV* wave case, both compressional force and vertically-directed force are considered.

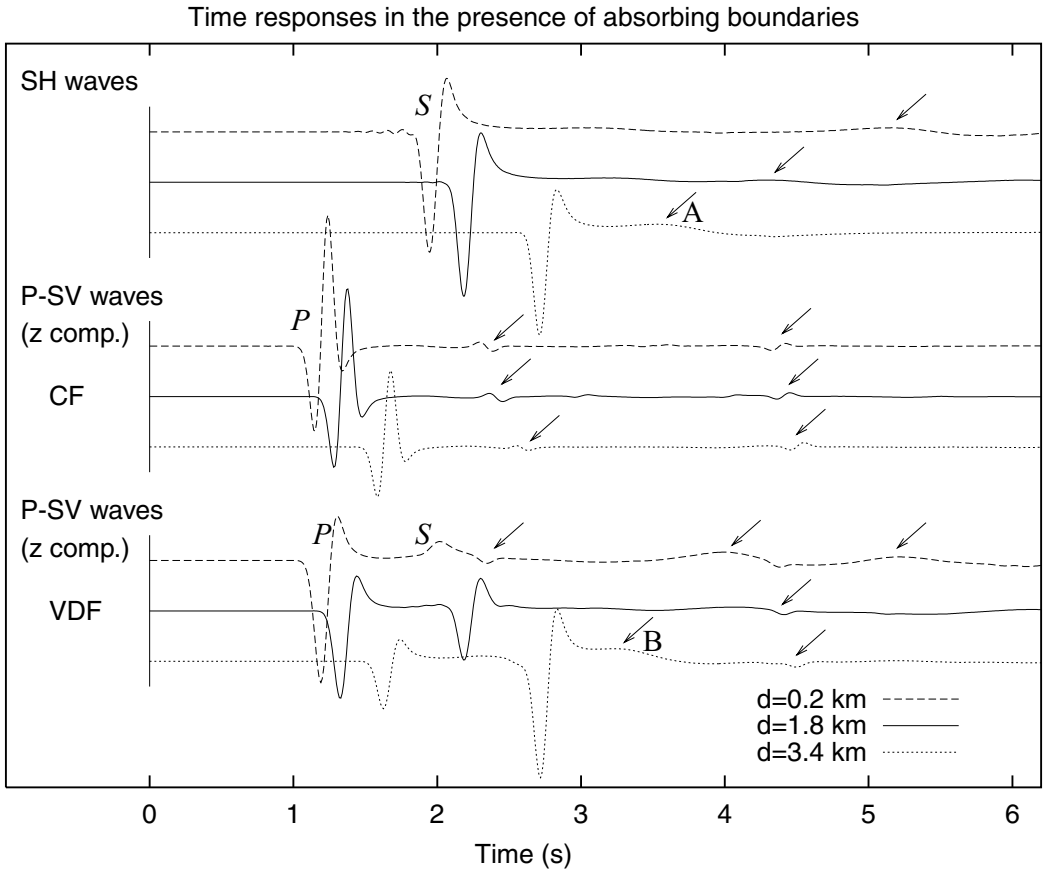

Figure 6. Time responses of *SH* and *P–SV* waves (vertical component) at three receivers (A_j, $j = 1, 2, 3$ in Fig. 3) in homogeneous media with four absorbing boundaries. For a test in *P–SV* waves, both compressional force (CF) and vertically-directed force (VDF) are considered. Some spurious waves are indicated by arrows. The features at A. B are discussed in the text.

$$Q_j(i_x, i_z) = \mathcal{A}_x\left[e^{\mathcal{B}_x i_x^2} + e^{\mathcal{B}_x (i_x - N_x)^2}\right] + \mathcal{A}_z\left[e^{\mathcal{B}_z (i_z + 20)^2} + e^{\mathcal{B}_z (i_z - N_z + 20)^2}\right], \qquad j = x, y, z, \qquad i_x = 1, 2, \ldots, N_x, \qquad i_z = 1, 2, \ldots, N_z. \quad (45)$$

The numerical model has a width of 10 000 m and a height of 10 000 m, with a superimposed 128-by-128 grid. The shear wave velocity β is 1.8 km s^{-1} and the density in the medium is 2.2 g cm^{-3}. The source is located at 1.5 km below the free surface (Fig. 3).

We compare numerical time responses with analytic solutions for three receivers with horizontal distances $d = 0.3, 2.6, 4.5$ km at depth at depth 2500 m (D_j, $j = 1, 2, 3$ in Fig. 3). The entire wavefields are composed of a direct phase (S) and a reflected phase (SS) from a free surface (Fig. 9) and they exhibit a good match with analytic solutions (Fig. 10).

4.3.2 P–SV waves: Lamb's problem

Lamb's problem (Lamb 1904) to find the Green's function for an isotropic elastic half-space with a traction-free boundary, is one of the classical problems in elastic wave propagation. Lamb's problem can be used to test the accuracy of numerical computation by checking the excitation of strong Rayleigh waves in the free surface on the uniform half-space by a surface source. This test can also be used to check the generation of coupled phases, head waves and Rayleigh waves at a free surface by implementing explosive source inside an homogeneous medium (sometimes called Garvin's (1956) problem). Kuhn (1985) studied the modelling of elastic wave propagation at various positions of the receivers for two kinds of sources, a buried compressional source and a vertically directed load on the surface. When spherical waves interact with a free surface boundary of a half-space, the incident waves are divided into three major types of waves: reflected waves from the boundary, head waves travelling with a body wave speed and Rayleigh waves decaying exponentially with depth.

To compare the analytic solutions with numerical results, analytic solutions based on Cagniard's technique (Burridge 1976; Pilant 1979) are convolved with a source time function $h(t)$. The applied source is an impulsive vertically directed force at depth 1.5 km. We use the same model as the *SH* wave problem with a compressional wave velocity α is 3.15 km s^{-1} (Fig. 3), and compare the numerical results with the analytic solutions for four receivers placed at the free surface. The epicentral distances for the receivers are 0.3, 1.5, 3.0 and 4.6 km (R_j, $j = 1, \ldots, 4$ in Fig. 3). The numerical time responses exhibit a good agreement with analytic solutions (Fig. 11). We note that the discrepancy in the later part of Rayleigh waves (C in Fig. 11) appearing in the time responses at the farthest receiver (R_4, $d = 4.6$ km) are related to the

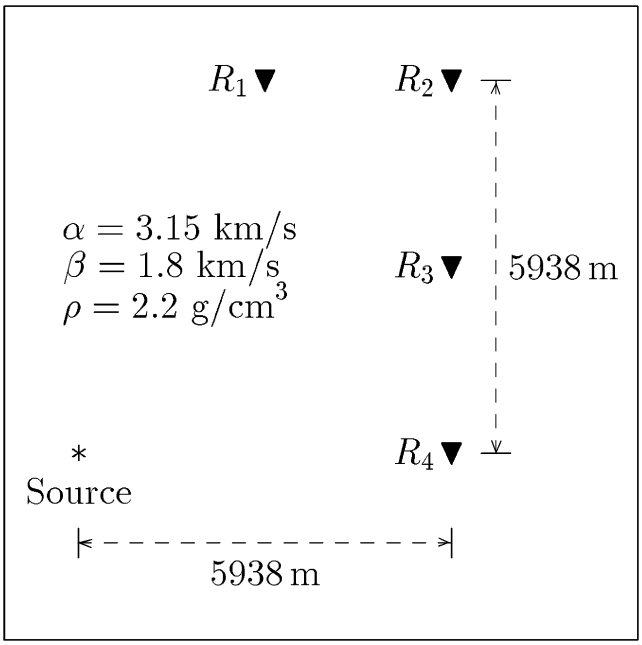

Figure 7. Description of a 2-D homogeneous unbounded medium and deployment of receivers (R_j, $j = 1, \ldots, 4$) with hypocentral distances from 5938 m to 8397 m.

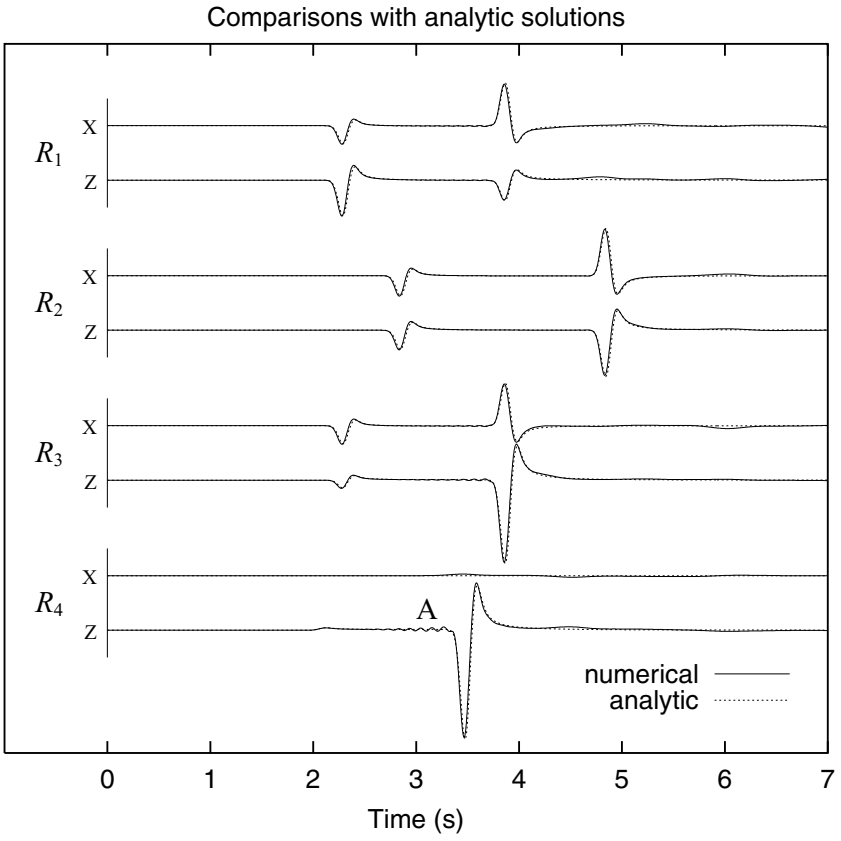

Figure 8. Comparisons between numerical time responses of *P–SV* waves with analytic solutions for four receivers in an homogeneous unbounded medium.

phenomenon discussed in Section 4.1 associated with reflections at the corners of the domain due to the strong gradients in the attenuation factors.

To compare the phase patterns, we collect time responses from receivers placed horizontally from $x = 0.94$ to 8.75 km at the free surface and at depth 2.5 km. For the receivers placed on a free surface, the recorded phases are the direct *P*, *S* waves, head waves (represented as *H*)

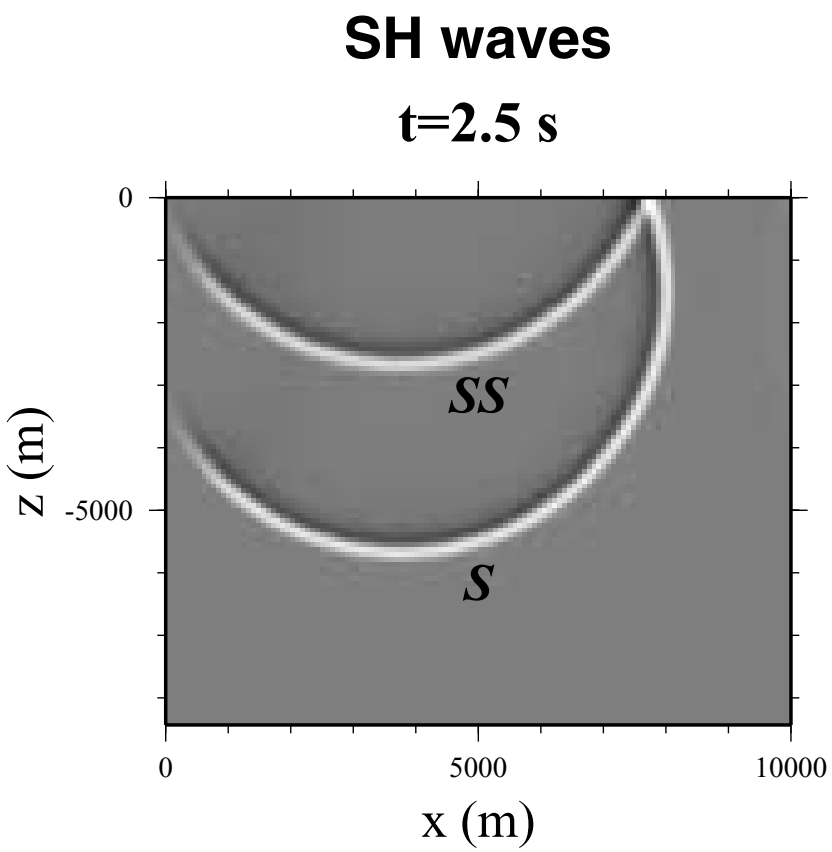

Figure 9. Snapshot of *SH* wave propagation in an homogeneous medium with a free surface at $t = 2.5$ s. The entire wavefields are composed of direct (*S*) and reflected (*SS*) phases.

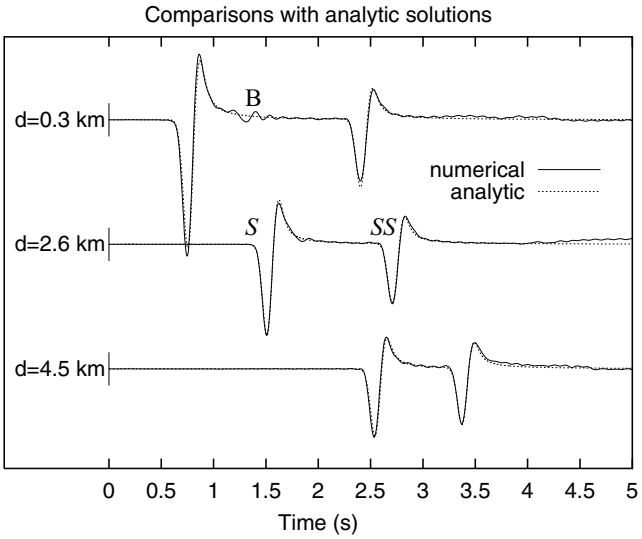

Figure 10. Comparisons of numerical time responses of *SH* waves with analytic solutions for three receivers (D_j, $j = 1, 2, 3$ in Fig. 3) in an homogeneous medium with a free surface. The receivers are placed horizontally at depth 2.5 km with distances $d = 0.3$, 2.6 and 4.5 km.

and Rayleigh waves (*R*) as shown in Fig. 12(a). When a depth of receivers is increased, the time responses become complex due to a phase coupling at the free surface. The discernible phases are *P*, *S*, *PP*, *PS*, *SP*, *SS* (Figs 12b and 13).

4.4 Two-layered heterogeneous media

The first model we consider for heterogeneous media cases is a two-layered media problem which has often been considered in the modelling of elastic wave propagation (Virieux 1986; Kelly *et al.* 1976). The medium has a horizontal internal boundary that divides it into two layers.

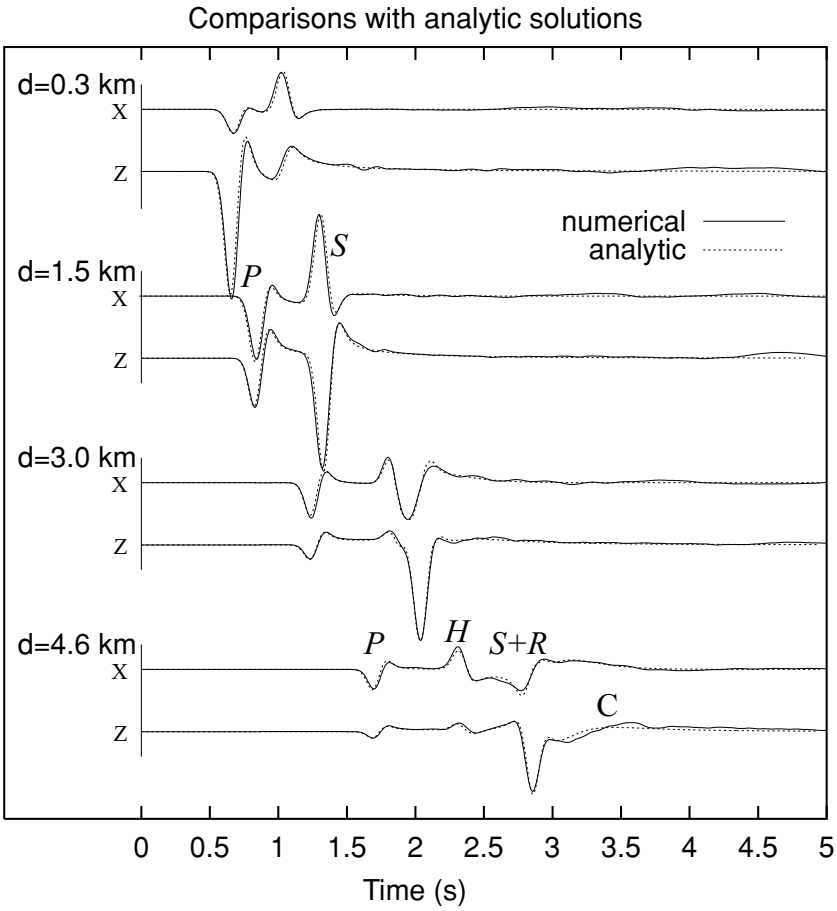

Figure 11. Comparison between numerical time responses of *P–SV* waves and analytic solutions for Lamb's problem at four free-surface receivers (R_j, $j = 1, \ldots, 4$ in Fig. 3) with epicentral distances $d = 0.3$, 1.5, 3.0 and 4.6 km. *H* represents head waves and *R* Rayleigh waves.

The compressional wave velocity (α_1) is 3.15 km s^{-1}, the shear wave velocity (β_1) is 1.8 km s^{-1} and the density is 2.2 g cm^{-3} in the top layer. The velocities in the bottom layer are twice those in the top layer ($\alpha_2 = 6.3$ km s^{-1}, $\beta_2 = 3.6$ km s^{-1}) and the density is 3.3 g cm^{-3} (Fig. 14). The width and height of the model are all 10 000 m and an internal boundary is placed at depth 3000 m. The point force is applied at $x = 3750$ m, $z = 1500$ m. We apply a point source in the *SH* wave case and a compressional point source for the *P–SV* wave case to simplify the wavefields in media.

For a check of numerical accuracy in the media, we present a comparison between numerical time responses for *SH* wave case with analytic solutions (Aki & Richards 1980) in the absence of free surface to avoid multireflected phases from a free surface. Since, however, it is difficult to obtain an 'exact' analytic solution for *P–SV* wave case due to a phase coupling at boundaries, we consider numerical modelling and features of elastic wave propagation in the media with a free surface.

4.4.1 SH waves

First, we check the numerical accuracy of a wavelet-based method in a two-layered heterogeneous medium with four absorbing boundaries at the edges of the domain. The numerical time responses at three receivers deployed horizontally at depth 1030 and 1970 m with horizontal distances $d = 310$, 1480, 2270, 3050, 3830 m (R_j, $j = 1, \ldots, 5$ in Fig. 14) are compared with analytic solutions. The phases in the time responses are direct *S*, reflected *S* and head waves. The comparisons in Fig. 15 show a good match for head waves and direct phases (*S*), head waves (represented as *H* in the Figure) and reflected phases (*Sr* in the Figure).

The entire wavefields in two-layered media without a free surface are composed of direct *S* phases, opposite-phase reflected phases (*Sr*), in-phase transmitted phases (*St*), head waves (*H*) and interface waves (*I*, Pilant 1972) at the internal boundary (Fig. 16). The head waves develop from the internal boundary by connecting a transmitted phase to a reflected phase, and propagate to the upper layer with velocity β_1. Also, the interface waves develop at the internal boundary where the physical parameters are changed suddenly, and propagate following the interface. The interface waves show the non-dispersive waveform and decay exponentially with depth like surface waves.

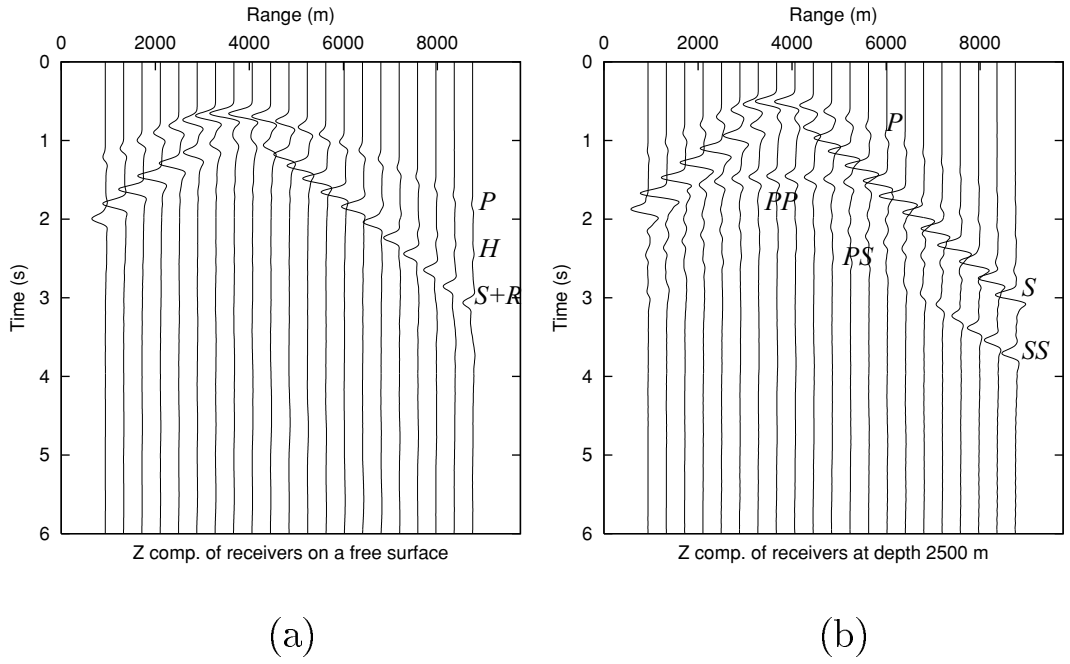

Figure 12. Numerical time responses (vertical components) of *P–SV* elastic wave propagation in an homogeneous medium recorded at 21 receivers placed horizontally (a) on a free surface and (b) at depth 2500 m, the main seismic phases are indicated.

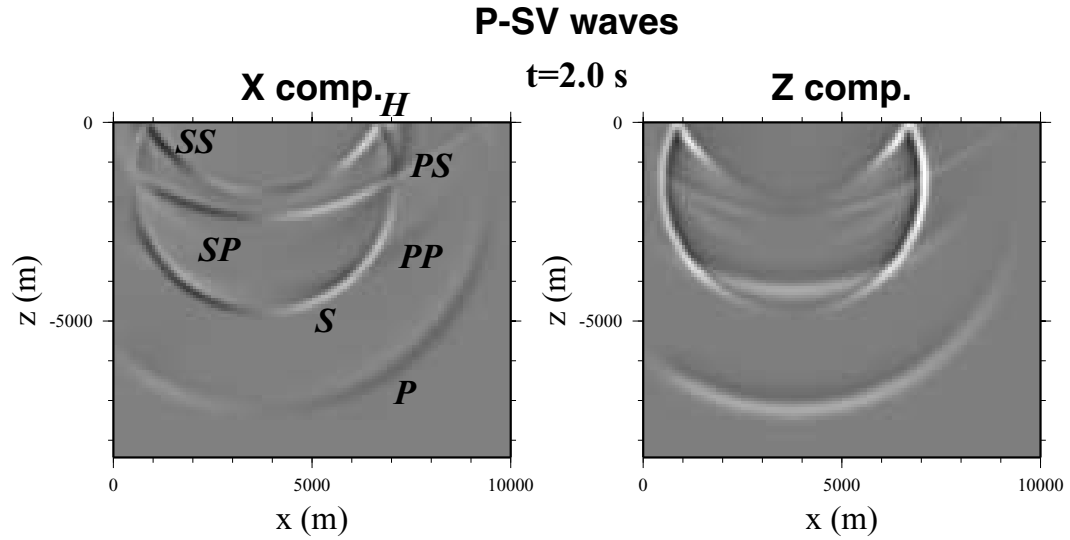

Figure 13. Snapshot of *P–SV* wave propagation in an homogeneous medium with a free surface (Lamb's problem) at $t = 2.0$ s.

4.4.2 P–SV waves

An explosive point source which generates only *P* waves is applied in the two layered heterogeneous media with a free surface for convenience in identification of phases. As a result of phase coupling at the boundaries, the wavefields are complicated and the entire wavefields are composed of direct *P* waves, reflected *P* and *S* waves from the internal boundary (represented as *PPr* and *PSr* in Fig. 17) and the free surface (*PP*, *PS*), transmitted *P* and *S* waves at the internal boundary (*PPt*, *PSt*), head waves (*Ht*, *Hrp*, *Hrs*) and interface waves. Note that various head waves are generated at the free surface and the internal boundary. At the internal boundary, the head waves connect the reflected phases with transmitted phases (e.g. *Hrp*, *Hrs*) or both transmitted (or, reflected) phases each other (e.g. *Ht*), and they propagate to upper or lower layer with a body wave velocity from the internal boundary.

4.5 Media with a general linear gradient in seismic properties

As a further, more complex example we consider a model with a slanted linear gradient in seismic properties (Fig. 18). We construct the model by setting the velocities and the density to increase linearly in both the vertical and horizontal coordinates. This linear gradient model

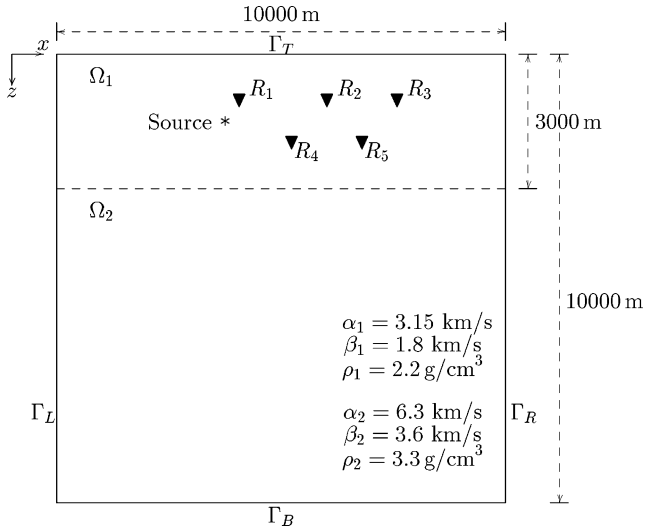

Figure 14. Description of two-layered heterogeneous elastic media with a planar internal boundary at depth 3000 m. The elastic wave velocities in a bottom layer are twice of those in a top layer. Five receivers (R_j, $j = 1, \ldots, 5$) are placed horizontally at depth 1030 and 1970 m to collect time responses of *SH* waves for comparisons with analytic solutions.

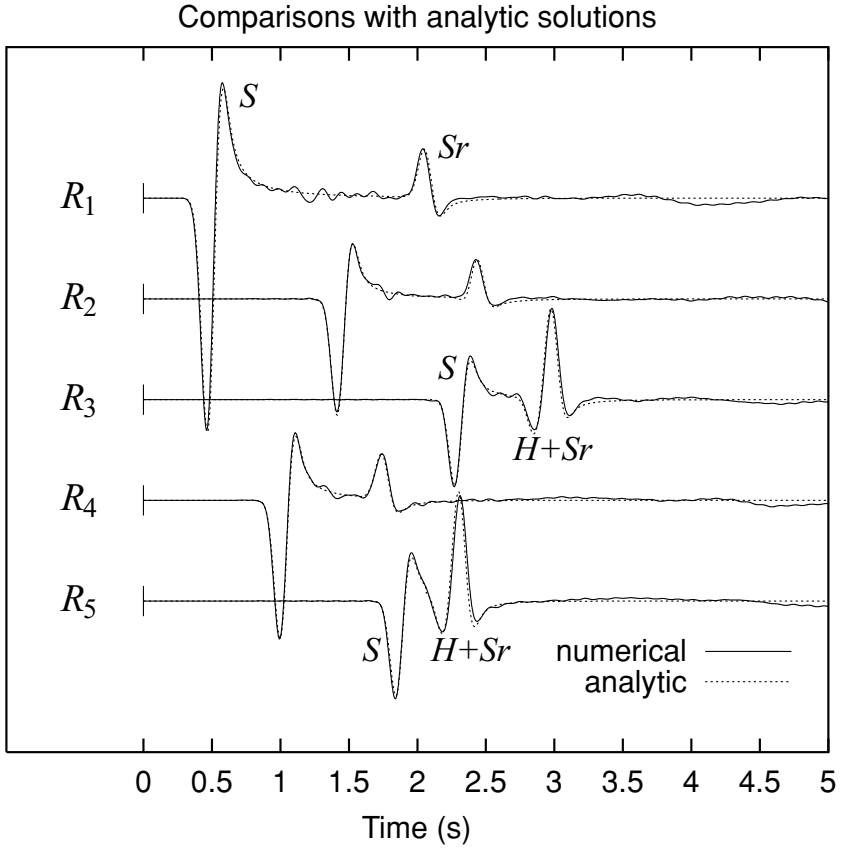

Figure 15. Comparisons between numerical time responses of *SH* waves and analytic solutions for two-layered media problem at five receivers (R_j, $j = 1, \ldots, 5$ in Fig. 14) with horizontal distances $d = 310$, 1480, 2270, 3050 and 3830 m at depth 1030 and 1970 m. *H* stands for head waves and *Sr* for reflected waves from a internal boundary.

provides a good test of the wavelet-based scheme in a model without symmetries in the expected wave front behaviour. The top layer is set to be homogeneous and the artificial boundary over the top layer is considered as a free surface (Fig. 18). The compressional wave velocity (α) ranges from 3.15 to 7.88 km s^{-1}, the shear wave velocity (β) from 1.8 to 4.5 km s^{-1}, the density (ρ) from 2.2 to 3.85 g cm^{-3}, and the angle of the slanted velocity structure is 38.7° (Fig. 18). We consider *P–SV* wave propagation in this model with a vertically-directed force applied at (3750 m, 1500 m).

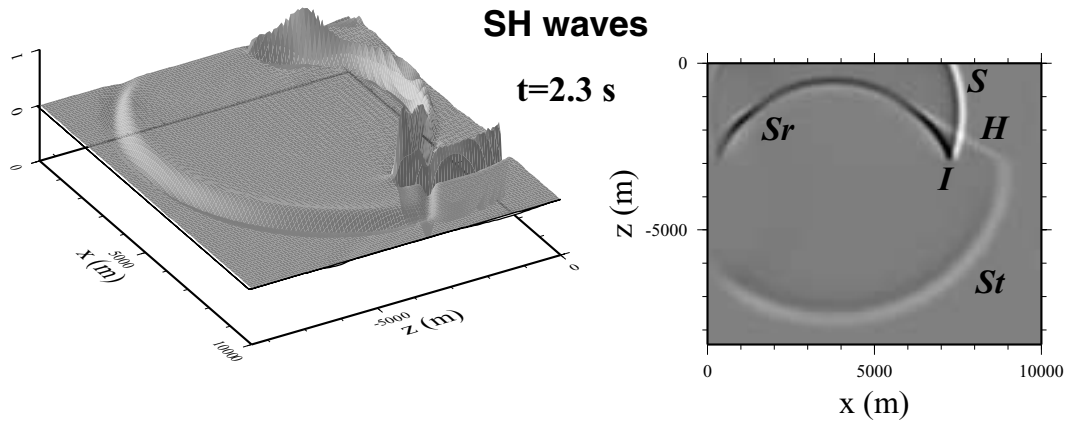

Figure 16. Snapshot of *SH* wave propagation in two-layered media at $t = 1.8$ s. The entire wavefields are composed of direct waves (*S*), reflected waves (*Sr*), transmitted waves (*St*), head waves (*H*) and interface waves (*I*) at the boundary.

As the velocities increase with both depth and distance, the shape of wavefields becomes elliptic towards the bottom right in Fig. 19. Since the velocity in media increase gradually, there are no significant reflected phases or head waves at the internal boundary. Therefore, entire wavefields are composed of direct phases (*P*, *S*) and reflected phases from a free surface (*PP*, *PS*, *SP*, *SS*), head waves (*H*) and Rayleigh wave (*R* in Fig. 20), like Lamb's problem in Section 4.3.2. The time responses at receivers on a free surface and at depth 2500 m in Fig. 20 show that the phases arrive faster than those in Lamb's problem (Fig. 12).

We also note that the composite waves of *S* and Rayleigh waves in Fig. 20(a) exhibit larger amplitude of waves compared to those in homogeneous medium in Fig. 12(a) because the wave velocities of media in Fig. 18 are increased gradually from $x = 7500$ m at the free surface and the phases are not attenuated with distance much compared to an homogeneous medium case.

4.6 Random heterogeneous media

Up to now, we have tested the wavelet-based method in simple models and shown that the method could generate good numerical responses. However, the 'real' Earth has a significant variation in its mineral composition and grain size distribution due to chemical activity with depth or tectonic processes, e.g. folding, faulting (Sato & Fehler 1998). As a result, these variations form strongly heterogeneous media in the lithosphere with the spatial variation of physical properties such as velocities and density. These wide spatial variation of elastic properties in the lithosphere was revealed by various geophysical and seismic studies. Also, the irregular heterogeneity in a region about 200 km thick above the core–mantle boundary was revealed through seismic records (Kennett 1983).

Even if the numerical results exhibit good agreements with analytic solutions in simple models, one can't guarantee that the method can generate the reliable numerical responses in 'real' Earth with often large variations of physical parameters because numerical methods based on discretized grid points, such as finite difference and finite element methods, are not affected much in accuracy in regularized heterogeneous media (e.g. two-layered media). Sato & Fehler (1998) indicated that the grid-based schemes approximate the responses of the waves through averages over many gridpoints in calculating spatial derivatives. As an evidence, they provided a phenomenon in finite-difference simulation that the numerical responses do not exhibit correct phase amplitudes in heterogeneous media, while display accurate phase-arrival times. Therefore, the method becomes unstable in highly perturbed media.

Therefore, we introduce a highly perturbed medium with maximum 20 per cent perturbation on physical parameters which can be expected in 'real' Earth and the usual grid-based methods often fail to compute responses. By testing the stability of the wavelet-based method which can compute spatial derivative exactly and stably, we show the possibility of the method as a tool for the 'real' Earth. For the construction of a perturbed medium, we follow a scheme in Roth & Korn (1993). For more details, we refer to Roth & Korn (1993) and Sato & Fehler (1998).

Fig. 21 shows the stochastic perturbation of *P* and *S* wave velocities added to background homogeneous medium with $\alpha = 3.15$ km s^{-1}, $\beta = 1.8$ km s^{-1} and $\rho = 2.2$ g cm^{-3}. The systematic spatial perturbation in medium is considered by implementing the Von Karman autocorrelation function with a correlation distance $a = 10$ km. We implement a compressional point force inside a medium at (3750 m, 5500 m). The entire wavefields are composed of direct phase (*P*), reflected waves (*PP*, *PS*) from a free surface and various complex back-scattered waves (Fig. 22). Also, due to the generation of back-scattered waves, the main phases exhibit the apparent attenuation during propagation in the media. The numerical responses in the random medium are compared with those in the homogeneous medium in Fig. 23. The numerical responses with large amplitudes of back-scattered waves are stable throughout computation (Fig. 23).

These numerical calculations using the wavelet scheme illustrate the resilience of both *P* and *S* wave fronts in the presence of strong heterogeneity. Significant coda waves are shed and there are local perturbations of the wave fronts, but the dents are soon infilled by 'wave

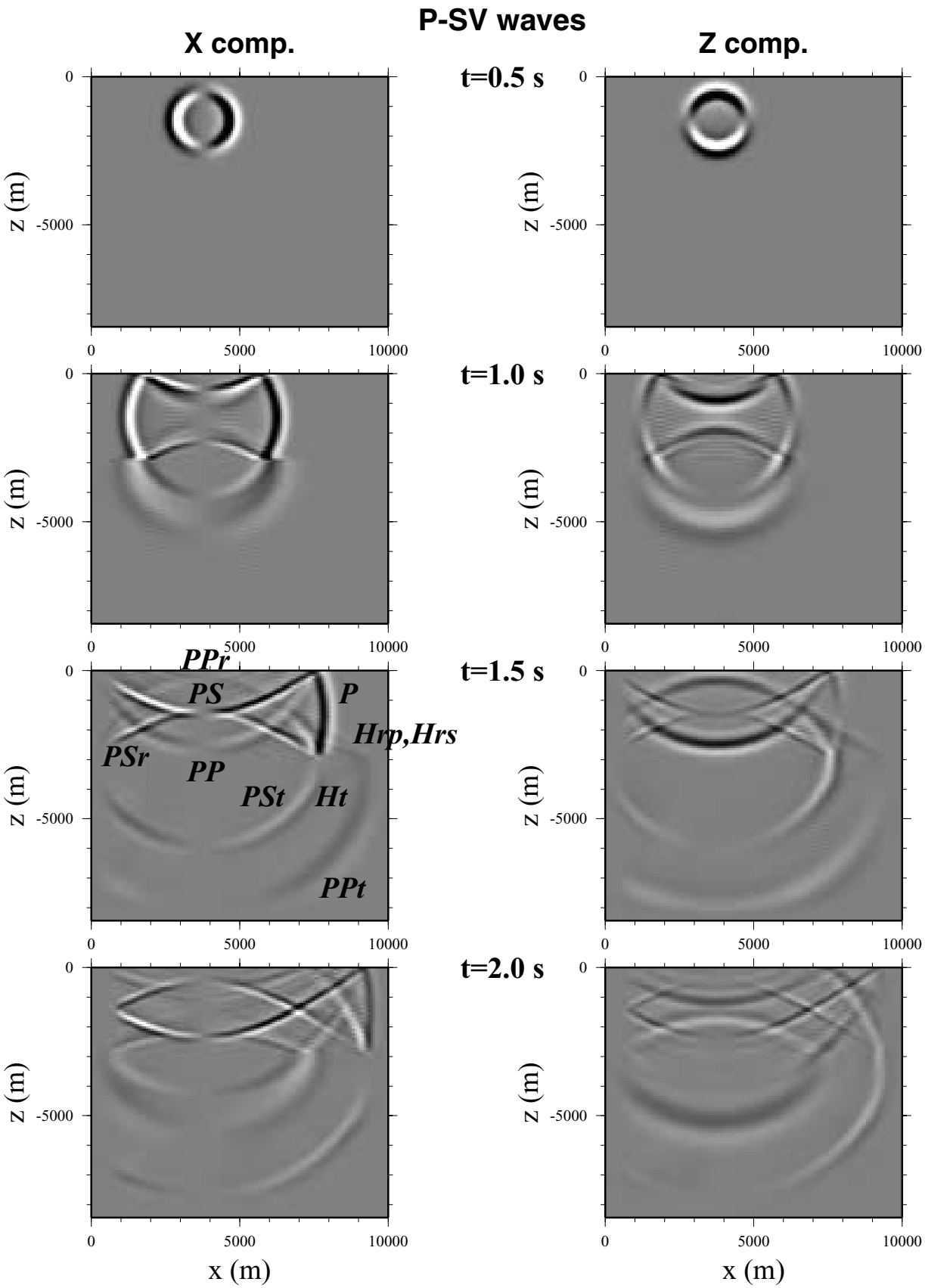

Figure 17. Snapshot of *P–SV* wave propagation in two-layered media with compressional point force inside a top layer at $t = 0.5$, 1.0, 1.5 and 2.0 s. The entire wavefields are composed of direct phases (*P*, *S*), reflected waves from the internal boundary (*PPr, PSr*) or the free surface (*PP, PS*), various head waves (e.g. *Hrp, Hrs, Ht*) and interface waves.

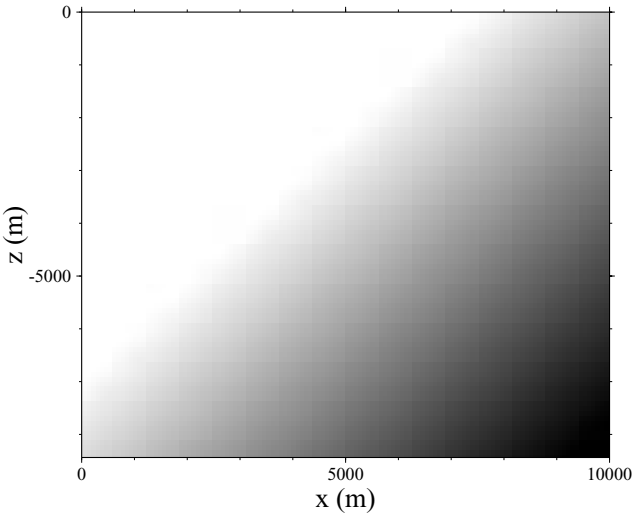

Figure 18. Distribution of compressional and shear wave velocities (α, β) and a density (ρ) on heterogeneous media. The velocity structure is slanted by 38.7° and the elastic wave velocity and the density increase linearly with depth and distance. The compressional wave velocity ranges from 3.15 to 7.88 km s^{-1}, the shear wave velocity from 1.8 to 4.5 km s^{-1} and the density from 2.2 to 3.85 g cm^{-3}.

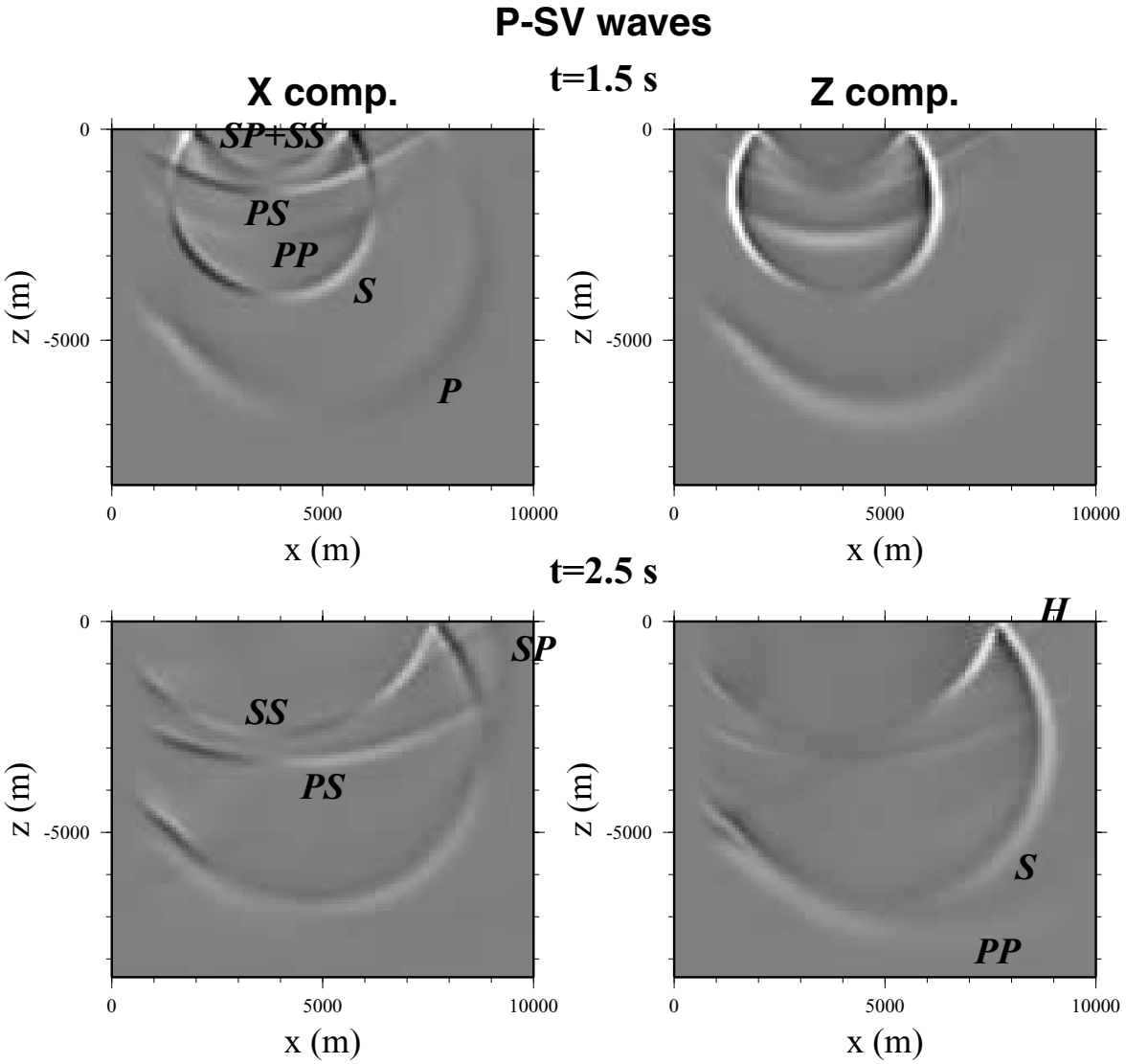

Figure 19. Snapshot of *P–SV* wave propagation in the linear gradient velocity media at $t = 1.5$ and 2.5 s. The wavefields are distorted by the influence of the gradient.

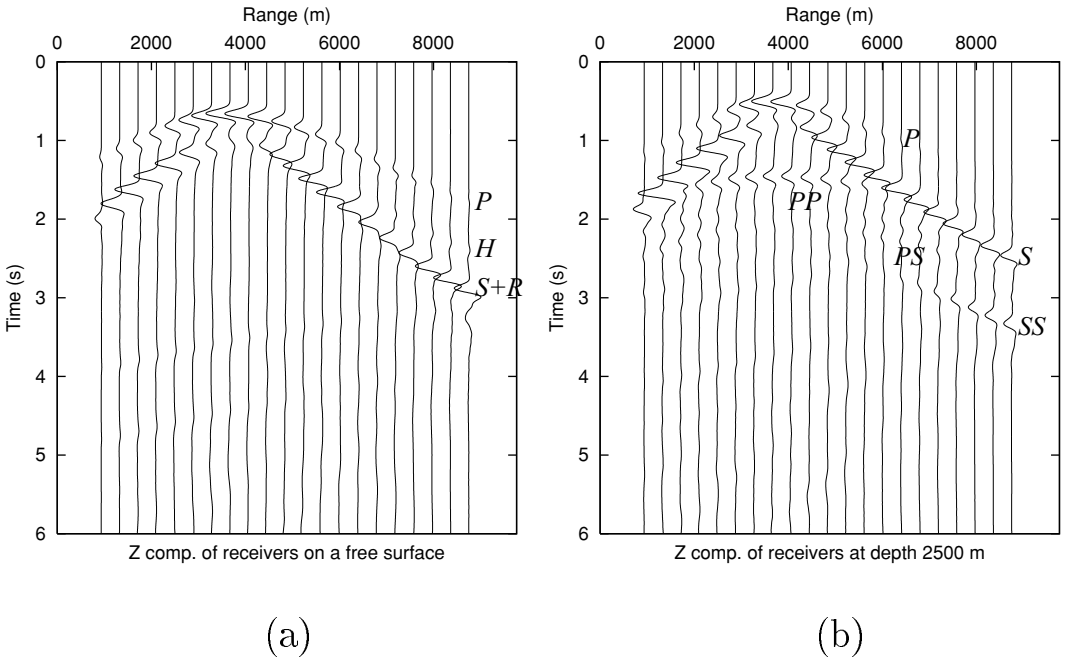

Figure 20. Numerical time responses of *P–SV* waves (vertical components) in linear gradient velocity media recorded at 21 receivers placed horizontally (a) on a free surface and (b) at depth 2500 m.

front healing' (see Igel & Gudmundsson 1997). There is some redistribution of amplitude, but the major phases are recognizable in Figs 22, 23 despite the substantial variations in medium properties (Fig. 21).

5 DISCUSSION AND CONCLUSIONS

The wavelet-based method has been introduced for numerical modelling of an elastic wave propagation in 2-D media problems. The scheme represents spatial differentiation operators through wavelet bases and the resulting second-order differential equations for time are treated by a displacement-velocity formalism and a semi-group approach.

The wavelet method for a spatial differentiation is not a grid-based scheme in the physical domain like a Fourier method although sampling is needed at given points. Therefore, we can maintain an accuracy of computation of spatial derivative uniformly throughout a whole domain in contrast to usual grid methods such as the FD scheme that cumulates numerical errors during computation of derivative terms from grid to grid.

The displacement-velocity formulation recasts the elastic wave equations in a form where the semi-group approach precisely developed for a parabolic PDE can be employed. Using a Taylor expansion, a recursive discrete solution can be computed by approximating an exponential function with a linear operator matrix in the exponent. The traction-free boundary is treated by an equivalent force term in the semi-group

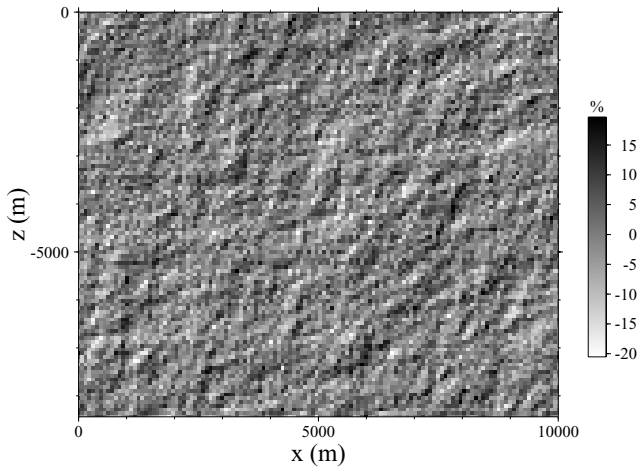

Figure 21. A representation of a Gaussian random perturbation of velocities using a Von Karman autocorrelation function.

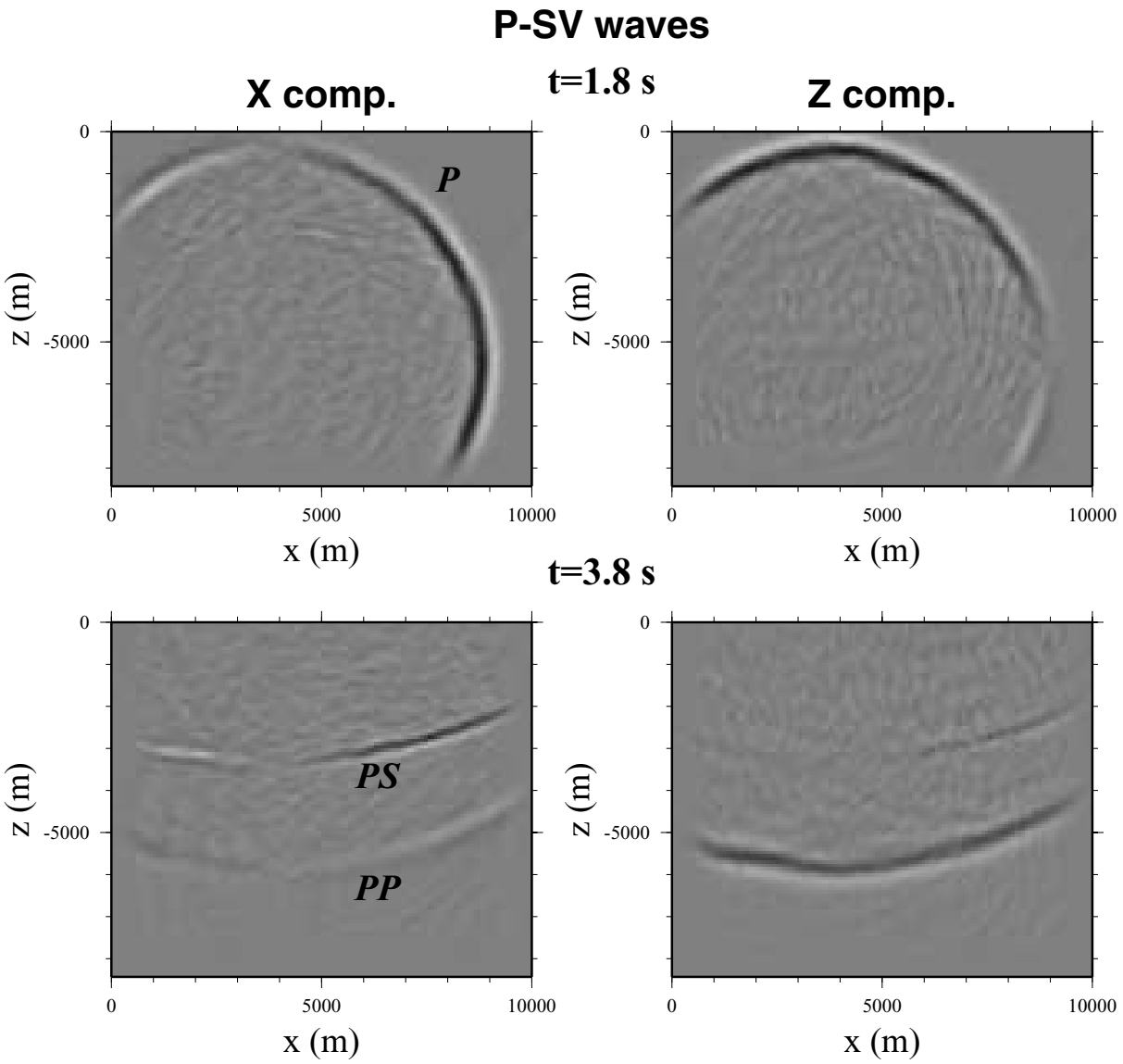

Figure 22. Snapshot of *P–SV* wave propagation for a compressional point force in a stochastic heterogeneous medium with a Gaussian random perturbation in Fig. 21 at $t = 1.8$ and 3.8 s. The back-scattered phases develop after the direct phase *P* and the reflected phases (*PP, PS*) from a free surface exhibit distorted wavefronts.

approach, leading to a stable implementation of the boundary conditions. We expect that other boundary conditions which are needed in complex models, such as a cavity inside media, can be considered in a similar stable way using the semi-group approach. The inclusion of attenuation factors for treating artificial boundaries in elastic wave equations reduced the cost of computation by allowing the use of smaller domains.

For classical 2-D problems, we have compared the numerical results with analytic solutions and we studied the accuracy of the method. The method is not only stable during numerical computation, but also has achieved quite good results in various comparisons. Also, we introduced two simple heterogeneous models and highly perturbed random media to test the capability of the method. The wavelet-based method works well not only in the case of sudden variation of physical parameters at a boundary, but also for linear gradients where physical parameters are changing continuously. Moreover, the method provided the stable time responses in a highly perturbed medium. We expect the method can be extended to complex stochastic media problems where accurate treatments of spatial derivatives are essential for stable modelling.

REFERENCES

Aki, K. & Richards, P.G., 1980. *Quantitative Seismology, Theory and Methods,* Vol. 1, W.H. Freeman and Company, San Francisco.

Alford, R.M., Kelly, K.R. & Boore, D.M., 1974. Accuracy of finite-difference modeling of the acoustic wave equation, *Geophysics*, **39**, 834–842.

Anant, K.S. & Dowla, F.U., 1997. Wavelet transform methods for phase identification in three-component seismograms, *Bull. seism. Soc. Am.,* **87,** 1598–1612.

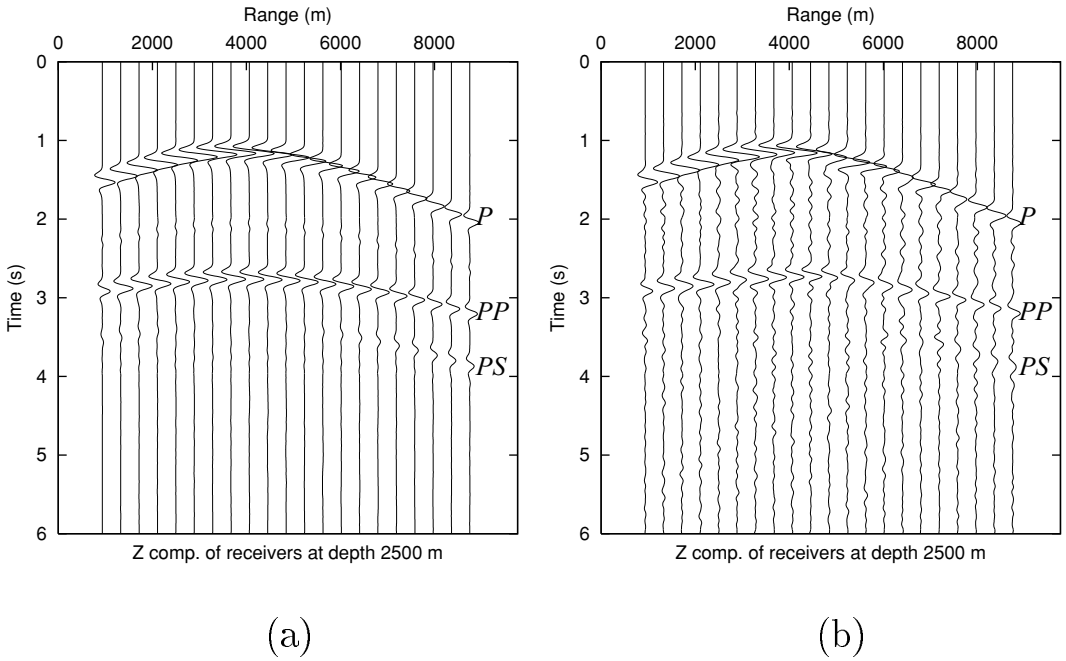

Figure 23. Comparison between numerical time responses of *P–SV* waves (vertical components) (a) in an homogeneous medium and (b) in a stochastic heterogeneous medium. The 21 receivers are placed horizontally at depth 2500 m.

Augenbaum, J.M., 1992. The pseudo-spectral method for limited-area elastic wave calculations, in *Computational Methods in Geosciences,* eds W.E. Fitzgibbon & M.F. Wheeler, SIAM, Philadelphia.

Bayliss, A., Jordan, K.E., Lemesurier, B.J. & Turkel, E., 1986. A fourth-order accurate finite-difference scheme for the computation of elastic waves, *Bull. seism. Soc. Am.,* **76,** 1115–1132.

Bear, L.K. & Pavlis, G.L., 1997. Estimation of slowness vectors and their uncertainties using multi-wavelet seismic array processing, *Bull. seism. Soc. Am.,* **87,** 755–769.

Bear, L.K. & Pavlis, G.L., 1999. Multi-channel estimation of time residuals from broad band seismic data using multi-wavelets, *Bull. seism. Soc. Am.,* **89,** 681–692.

Belleni-Morante, A., 1979. *Applied Semigroups and Evolution Equations,* Oxford University Press, Oxford.

Ben-Menahem, A. & Singh, S.J., 1981. *Seismic Waves and Sources,* Springer-Verlag, Berlin.

Beylkin, G., 1992. On the representation of operators in bases of compactly supported wavelets, *SIAM J. Numer. Anal.,* **6,** 1716–1740.

Beylkin, G. & Keiser, J.M., 1997. On the adaptive numerical solution of nonlinear partial differential equations in wavelet bases, *J. Comp. Phys.,* **132,** 233–259.

Beylkin, G., Keiser, J.M. & Vozovoi, L., 1998. A new class of time discretization schemes for the solution of nonlinear PDEs, *J. Comput. Phys.,* **147,** 362–387.

Burridge, R., 1976. *Some Mathematical Topics in Seismology,* Courant Institute of Mathematical Sciences, New York University, New York.

Carcione, J.M., 1994. The wave equation in generalized coordinates, *Geophysics,* **59,** 1911–1919.

Cerjan, C., Kosloff, D., Kosloff, R. & Reshef, M., 1985. A nonreflecting boundary condition for discrete acoustic and elastic wave equations, *Geophysics,* **50,** 705–708.

Chan, Y.T., 1995. *Wavelet Basics,* Kluwer Academic Publishers, Boston.

Clayton, R. & Engquist, B., 1977. Absorbing boundary conditions for acoustic and elastic wave equations, *Bull. seism. Soc. Am.,* **67,** 1529–1540.

Daubechies, I., 1992. *Ten Lectures on Wavelets,* Society for industrial and applied mathematics, Philadelphia, Pennsylvania.

Faccioli, E., Maggio, F., Quarteroni, A. & Tagliani, A., 1996. Spectral-domain decomposition methods for the solution of acoustic and elastic wave equations, *Geophysics,* **61,** 1160–1174.

Frankel, A., 1993. Three-dimensional simulations of ground motions in the san bernardino valley, california, for hypothetical earthquakes on the san andreas fault, *Bull. seism. Soc. Am.,* **83,** 1020–1041.

Garvin, W.W., 1956. Exact transient solution of the buried line source problem, *Proc. Royal Soc. London, Series A,* **234,** 528–541.

Gottlieb, D., Gunzburger, M. & Turkel, E., 1982. On numerical boundary treatment of hyperbolic systems for finite-difference and finite element methods, *SIAM J. Numer. Anal.,* **19,** 671–682.

Graves, R.W., 1996. Simulating seismic wave propagation in 3D elastic media using staggered-grid finite differences, *Bull. seism. Soc. Am.,* **86,** 1091–1106.

Holmström, M., 1999. Solving hyperbolic PDEs using interpolating wavelets, *SIAM J. Sci. Comput.,* **21,** 405–420.

Hong, T.-K. & Kennett, B.L.N., 2002. On a wavelet-based method for the numerical simulation of wave propagation, *J. Comput. Phys.,* (in press).

Igel, H. & Gudmundsson, O., 1997. Frequency-dependent effects on travel times and waveforms of long-period *S* waves: implications for the scale of mantle heterogeneity, *Phys. Earth planet. Int.,* **104,** 229–246.

Kelly, K.R., Ward, R.W., Treitel, S. & Alford, R.M., 1976. Synthetic seismograms: a finite-difference approach, *Geophysics,* **41,** 2–27.

Kennett, B.L.N., 1983. *Seismic Wave Propagation in Stratified Media,* Cambridge University Press, Cambridge.

Kennett, B.L.N., 1988. Radiation from a moment-tensor source, in *Seismological Algorithm, Computational Methods and Computer Programs,* ed. Doornbos, D.J., Academic Press Inc., San Diego.

Komatitsch, D. & Tromp, J., 1999. Introduction to the spectral element method for three-dimensional seismic wave propagation, *Geophys. J. Int.,* **139,** 806–822.

Komatitsch, D. & Vilotte, J.-P., 1998. The spectral element method: an efficient tool to simulate the seismic response of 2D and 3D geological structures, *Bull. seism. Soc. Am.,* **88,** 368–392.

Kosloff, R. & Kosloff, D., 1986. Absorbing boundaries for wave propagation problems, *J. Comput. Phys.,* **63,** 363–376.

Kosloff, D., Reshef, M. & Loewenthal, D., 1984. Elastic wave calculations by the fourier method, *Bull. seism. Soc. Am.,* **74,** 875–891.

Kosloff, D., Kessler, D., Filho, A.Q., Tessmer, E., Behle, A. & Strahilevitz, R., 1990. Solution of the equations of dynamic elasticity by a Chebychev spectral method, *Geophysics,* **55,** 734–748.

Kuhn, M.J., 1985. A numerical study of lamb's problem, *Geophys. Prospect.,* **33,** 1103–1137.

Lamb, H., 1904. On the propagation of tremors over the surface of an elastic solid, *Phil. Trans. R. Soc. Lond.,* A., **203,** 1–42.

Lewalle, J., 1998. Formal improvements in the solution of the wavelet-transformed possion and diffusion equations, *J. Math. Phys.,* **39,** 4119–4128.

Lilly, J.M. & Park, J., 1995. Multiwavelet spectral and polarization analysis of seismic records, *Geophys. J. Int.,* **122,** 1001–1021.

Mahrer, K.D., 1990. Numerical time step instability and Stacey's and Clayton-Engquist's absorbing boundary conditions, *Bull. seism. Soc. Am.,* **80,** 213–217.

Moczo, P., 1998. *Introduction To Modeling Seismic Wave Propagation By the Finite-Difference Method,* Lecture Notes, Disaster Prevention Research Institute, Kyoto University.

Moczo, P., Bystricky, E., Kristek, J., Carcione, J.M. & Bouchon, M., 1997. Hybrid modeling of P–SV seismic motion at inhomogeneous viscoelastic topographic structures, *Bull. seism. Soc. Am.,* **87,** 1305–1323.

Ohminato, T. & Chouet, B.A., 1997. A free-surface boundary condition for including 3D topography in the finite-difference method, *Bull. seism. Soc. Am.,* **87,** 494–515.

Pilant, W.L., 1972. Complex roots of the stoneley-wave equation in the finite-difference method, *Bull. seism. Soc. Am.,* **62,** 285–299.

Pilant, W.L., 1979. *Elastic Waves in the Earth,* Elsevier, New York.

Roth, M. & Korn, M., 1993. Single scattering theory versus numerical modelling in 2-D random media, *Geophys. J. Int.,* **112,** 124–140.

Sato, H. & Fehler, M.C., 1998. *Seismic Wave Propagation and Scattering in the Heterogeneous Earth,* Springer-Verlag, New York.

Shensa, M.J., 1992. The discrete wavelet transform: wedding the À trous and mallat algorithms, *IEEE Trans. on Signal Processing,* **40,** 2464–2482.

Sochacki, J., Kubichek, R., George, J., Fletcher, W.R. & Smithson, S., 1987. Absorbing boundary conditions and surface waves, *Geophysics,* **52,** 60–71.

Stacey, R., 1988. Improved transparent boundary formulations for the elastic-wave equation, *Bull. seism. Soc. Am.,* **78,** 2089–2097.

Strang, G. & Nguyen, T., 1996. *Wavelets and Filter Banks,* Wellesley-Cambridge Press, Wellesley, USA.

Tal-Ezer, H., Kosloff, D. & Koren, Z., 1987. An accurate scheme for seismic forward modelling, *Geophys. Prospect.,* **35,** 479–490.

Tessmer, E. & Kosloff, D., 1994. 3-D Elastic modeling with surface topography by a Chebychev spectral method, *Geophysics,* **59,** 464–473.

Thompson, K.W., 1990. Time-dependent boundary conditions for hyperbolic systems, II, *J. Comput. Phys.,* **89,** 439–461.

Tibuleac, M. & Herrin, E.T., 1999. An automatic method for determination of *Lg* arrival times using wavelet transforms, *Seism. Res. Lett.,* **70,** 577–595.

Vidale, J.E. & Clayton, R.W., 1986. A stable free-surface boundary condition for two-dimensional elastic finite-difference wave simulation, *Geophysics,* **51,** 2247–2249.

Virieux, J., 1984. *SH*-wave propagation in heterogeneous media: velocity-stress finite-difference method, *Geophysics,* **49,** 1933–1957.

Virieux, J., 1986. *P–SV* wave propagation in heterogeneous media: velocity-stress finite-difference method, *Geophysics,* **51,** 889–901.

Zahradnik, J., 1995. Simple elastic finite-difference scheme, *Bull. seism. Soc. Am.,* **85,** 1879–1887.

APPENDIX : DISCRETE TIME SOLUTION IN THE SOURCE REGION

Following eq. (21), we discretize the solution of elastic wave equations for the explicit case in a recursive form:

$$\mathbf{U}_{n+1} = e^{\delta t \mathbf{L}_h}\mathbf{U}_n + \delta t \boldsymbol{\beta}_0 \mathbf{F}_n, \tag{A1}$$

where $\mathbf{U}_n$ is a variable vector at a discretized time t_n, δt is a time step and $\boldsymbol{\beta}_0 = (e^{\delta t \mathbf{L}_h} - \mathbf{I})(\delta t \mathbf{L}_h)^{-1}$. $e^{\delta t \mathbf{L}_h}$ and $\boldsymbol{\beta}_0$ can be estimated using a Taylor expansion as shown in eq. (22). Using a linear matrix operator $\mathbf{L}_h$ in eq. (20), $\mathbf{L}_h^2$ and $\mathbf{L}_h^3$ are given by

$$\mathbf{L}_h^2 = \begin{pmatrix} \mathcal{L}_{xx}^h & 0 & \mathcal{L}_{xz}^h & 0 \\ 0 & \mathcal{L}_{xx}^h & 0 & \mathcal{L}_{xz}^h \\ \mathcal{L}_{zx}^h & 0 & \mathcal{L}_{zz}^h & 0 \\ 0 & \mathcal{L}_{zx}^h & 0 & \mathcal{L}_{zz}^h \end{pmatrix}, \tag{A2}$$

and

$$\mathbf{L}_h^3 = \begin{pmatrix} 0 & \mathcal{L}_{xx}^h & 0 & \mathcal{L}_{xz}^h \\ \mathcal{L}_{xx}^h\mathcal{L}_{xx}^h + \mathcal{L}_{xz}^h\mathcal{L}_{zx}^h & 0 & \mathcal{L}_{xx}^h\mathcal{L}_{xz}^h + \mathcal{L}_{xz}^h\mathcal{L}_{zz}^h & 0 \\ 0 & \mathcal{L}_{zx}^h & 0 & \mathcal{L}_{zz}^h \\ \mathcal{L}_{zx}^h\mathcal{L}_{xx}^h + \mathcal{L}_{zz}^h\mathcal{L}_{zx}^h & 0 & \mathcal{L}_{zx}^h\mathcal{L}_{xz}^h + \mathcal{L}_{zz}^h\mathcal{L}_{zz}^h & 0 \end{pmatrix}. \tag{A3}$$

Therefore, $e^{\delta t \mathbf{L}_h}$ in eq. (22) can be written as

$$e^{\delta t \mathbf{L}_h} = \begin{pmatrix} I + \frac{\delta t^2}{2}\mathcal{L}_{xx}^h & \delta t I + \frac{\delta t^3}{6}\mathcal{L}_{xx}^h & \frac{\delta t^2}{2}\mathcal{L}_{xz}^h & \frac{\delta t^3}{6}\mathcal{L}_{xz}^h \\ \delta t \mathcal{L}_{xx}^h & I + \frac{\delta t^2}{2}\mathcal{L}_{xx}^h & \delta t \mathcal{L}_{xz}^h & \frac{\delta t^2}{2}\mathcal{L}_{xz}^h \\ \frac{\delta t^2}{2}\mathcal{L}_{zx}^h & \frac{\delta t^3}{6}\mathcal{L}_{zx}^h & I + \frac{\delta t^2}{2}\mathcal{L}_{zz}^h & \delta t I + \frac{\delta t^3}{6}\mathcal{L}_{zz}^h \\ \delta t \mathcal{L}_{zx}^h & \frac{\delta t^2}{2}\mathcal{L}_{zx}^h & \delta t \mathcal{L}_{zz}^h & I + \frac{\delta t^2}{2}\mathcal{L}_{zz}^h \end{pmatrix}. \tag{A4}$$

When $\gamma = 0$ (explicit case), $M = 1$ and the $\mathcal{L}^h_{ij}\mathcal{L}^h_{kl}$ terms ($i, j, k, l = x, z$) are ignored,

$$\beta_0 = (e^{\delta t \mathbf{L}_h} - \mathbf{I})(\delta t \mathbf{L}_h)^{-1} = \mathbf{I} + \frac{1}{2}\delta t \mathbf{L}_h + \frac{1}{6}\delta t^2 \mathbf{L}_h^2 + \frac{1}{24}\delta t^3 \mathbf{L}_h^3 + \cdots = \begin{pmatrix} I + \frac{\delta t^2}{6}\mathcal{L}^h_{xx} & \frac{\delta t}{2}I + \frac{\delta t^3}{24}\mathcal{L}^h_{xx} & \frac{\delta t^2}{6}\mathcal{L}^h_{xz} & \frac{\delta t^3}{24}\mathcal{L}^h_{xz} \\ \frac{\delta t}{2}\mathcal{L}^h_{xx} & I + \frac{\delta t^2}{6}\mathcal{L}^h_{xx} & \frac{\delta t}{2}\mathcal{L}^h_{xz} & \frac{\delta t^2}{6}\mathcal{L}^h_{xz} \\ \frac{\delta t^2}{6}\mathcal{L}^h_{zx} & \frac{\delta t^3}{24}\mathcal{L}^h_{zx} & I + \frac{\delta t^2}{6}\mathcal{L}^h_{zz} & \frac{\delta t}{2}I + \frac{\delta t^3}{24}\mathcal{L}^h_{zz} \\ \frac{\delta t}{2}\mathcal{L}^h_{zx} & \frac{\delta t^2}{6}\mathcal{L}^h_{zx} & \frac{\delta t}{2}\mathcal{L}^h_{zz} & I + \frac{\delta t^2}{6}\mathcal{L}^h_{zz} \end{pmatrix}. \tag{A5}$$

Therefore, eq. (21) can be approximated for the explicit case using (A4) and (A5):

$$\begin{pmatrix} u_x^{n+1} \\ v_x^{n+1} \\ u_z^{n+1} \\ v_z^{n+1} \end{pmatrix} = e^{\delta t \mathbf{L}_h} \begin{pmatrix} u_x^{n} \\ v_x^{n} \\ u_z^{n} \\ v_z^{n} \end{pmatrix} + \delta t \beta_0 \frac{1}{\rho} \begin{pmatrix} 0 \\ f_x^n \\ 0 \\ f_z^n \end{pmatrix}. \tag{A6}$$

APPENDIX : DISCRETE TIME SOLUTION IN THE MAIN REGION

When we consider the *P–SV* wave equations in the main region in which we include the body force effects through boundary conditions, we can write the governing equations as

$$\begin{aligned} \frac{\partial^2 u_x}{\partial t^2} &= \frac{1}{\rho}\left(\frac{\partial \sigma_{xx}}{\partial x} + \frac{\partial \sigma_{xz}}{\partial z}\right), \\ \frac{\partial^2 u_z}{\partial t^2} &= \frac{1}{\rho}\left(\frac{\partial \sigma_{xz}}{\partial x} + \frac{\partial \sigma_{zz}}{\partial z}\right), \end{aligned} \tag{B1}$$

where σ_{ij} ($i, j = x, z$) is a stress in (12). When eq. (B1) can be expressed in the first-order differential equation from as

$$\partial_t \mathbf{U} = \mathbf{L}\mathbf{U}, \tag{B2}$$

where $\mathbf{L}$ is a 4-by-4 matrix operator given by

$$\mathbf{L} = \begin{pmatrix} 0 & I & 0 & 0 \\ \mathcal{L}_{xx} & 0 & \mathcal{L}_{xz} & 0 \\ 0 & 0 & 0 & I \\ \mathcal{L}_{zx} & 0 & \mathcal{L}_{zz} & 0 \end{pmatrix}, \tag{B3}$$

and $\mathcal{L}_{ij}$ ($i, j = x, z$) is a scalar linear operator in (14). In this case, the discretized solution using a semi-group approach recursively is given by

$$\begin{pmatrix} u_x^{n+1} \\ v_x^{n+1} \\ u_z^{n+1} \\ v_z^{n+1} \end{pmatrix} = e^{\delta t \mathbf{L}} \begin{pmatrix} u_x^{n} \\ v_x^{n} \\ u_z^{n} \\ v_z^{n} \end{pmatrix}, \tag{B4}$$

where $e^{\delta t \mathbf{L}}$ can be expanded using a Taylor series:

$$e^{\delta t \mathbf{L}} = \begin{pmatrix} I + \frac{\delta t^2}{2}\mathcal{L}_{xx} & \delta t I + \frac{\delta t^3}{6}\mathcal{L}_{xx} & \frac{\delta t^2}{2}\mathcal{L}_{xz} & \frac{\delta t^3}{6}\mathcal{L}_{xz} \\ \delta t \mathcal{L}_{xx} & I + \frac{\delta t^2}{2}\mathcal{L}_{xx} & \delta t \mathcal{L}_{xz} & \frac{\delta t^2}{2}\mathcal{L}_{xz} \\ \frac{\delta t^2}{2}\mathcal{L}_{zx} & \frac{\delta t^3}{6}\mathcal{L}_{zx} & I + \frac{\delta t^2}{2}\mathcal{L}_{zz} & \delta t I + \frac{\delta t^3}{6}\mathcal{L}_{zz} \\ \delta t \mathcal{L}_{zx} & \frac{\delta t^2}{2}\mathcal{L}_{zx} & \delta t \mathcal{L}_{zz} & I + \frac{\delta t^2}{2}\mathcal{L}_{zz} \end{pmatrix}. \tag{B5}$$

APPENDIX : COEFFICIENTS OF *NS*-FORM OF OPERATOR ∂

When an operator T (e.g. derivative operator, convolution operator) is defined in $\mathbf{L}^2$ space, it can be represented in the tensor product bases (φ, ψ) and can form a matrix operator (in a standard form) expressing the operator T. With additional projection of the operated spaces on to the set of subspaces, Beylkin (1992) could express the operator as a non-standard form (*NS*-form) of matrix operator. The *NS*-form matrix operator can reduce the computational cost and makes the system including the operator simple to handle. For more detail of consideration of the operator in wavelet bases, we refer to Beylkin (1992).

In this study, we consider the derivative operator on wavelet bases and the coefficients of the *NS*-form of derivative operator (∂) can be obtained using (4.3) and (4.4) in Beylkin (1992). The coefficients (r_l^1, $-38 \leq l \leq 38$) of the first-order derivative operator are given by

$r_0^1 = 0$

$r_1^1 = -0.95122025816280881689532916709533637411 58$

$r_2^1 = 0.40924669691064934226928544889776754033222$

$r_3^1 = -0.21220235235817125241138778371057557905874$

$r_4^1 = 0.11174482984917235280645039046569709415 7023$

$r_5^1 = -0.05655635346747988268541634561994005024 1633$

$r_6^1 = 0.02679936774693490724310382908409417889846 21$

$r_7^1 = -0.01170202807403020480638436325828414863897 14$

$r_8^1 = 0.00465417919502178093224881196618884149408$

$r_9^1 = -0.00166934220231212180073645966992405276065193$

$r_{10}^1 = 0.00053477115388658414862943774657691290096661$

$r_{11}^1 = -0.00015143564780404289970142715147157287941 4476$

$r_{12}^1 = 0.00003746201279105294193528178559819939692 8948$

$r_{13}^1 = -7.98062612373177717451411878651423598602 46 \times 10^{-6}$

$r_{14}^1 = 1.43762532893493484270793311169125366450063 \times 10^{-6}$

$r_{15}^1 = -2.13704593950842754674837800413055144138844 \times 10^{-7}$

$r_{16}^1 = 2.53268333347132439070706272057383802194626 \times 10^{-8}$

$r_{17}^1 = -2.27480544299216844330375805979327460020808 \times 10^{-9}$

$r_{18}^1 = 1.44426541827778857728365870765027842747995 \times 10^{-10}$

$r_{19}^1 = -6.44180545408804973761027070941636085322 22 \times 10^{-12}$

$r_{20}^1 = 3.44564905561654405278246862627745978223022 \times 10^{-13}$

$r_{21}^1 = -1.70810862289007463312530040733908803206041 \times 10^{-14}$

$r_{22}^1 = -5.06690112450784489362459596079942138671 25 \times 10^{-15}$

$r_{23}^1 = 1.07728737053070114073883574318345357655184 \times 10^{-15}$

$r_{24}^1 = -2.06003417891317764387363040119484140295314 \times 10^{-17}$

$r_{25}^1 = -1.12743679605993942989302217522997280836838 \times 10^{-17}$

$r_{26}^1 = 4.71060297311839414353125611999646956301 9 \times 10^{-19}$

$r_{27}^1 = 5.85700050574045877225497015602900474268 49 \times 10^{-19}$

$r_{28}^1 = 9.52864329632444128153587652689488855420 51 \times 10^{-22}$

$r_{29}^1 = 2.20904986897211722029223908701950496319178 \times 10^{-24}$

$r_{30}^1 = 3.33571145835072113774507056021389203595443 \times 10^{-26}$

$r_{31}^1 = -7.43362314348887032978821852304852254979 06 \times 10^{-28}$

$r_{32}^1 = 6.39948774362356099915922695881574593381 84 \times 10^{-30}$

$r_{33}^1 = -2.73557349984210029408405391458398409911042 \times 10^{-32}$

$r_{34}^1 = -1.04765720469823213817922778531469877580904 \times 10^{-36}$

$r_{35}^1 = 3.47211905473434568099012621241871620336 94 \times 10^{-40}$

$r_{36}^1 = 1.27967643177469868693835368282035919724671 \times 10^{-44}$

$r_{37}^1 = -1.62422490373905792231749611455567746048172 \times 10^{-52}$

$$r_{38}^1 = 7.5979725818395493818388650700711955570933 \times 10^{-65}$$
$$r_{-j} = -r_j, \qquad 1 \le j \le 38, \tag{C1}$$

where the coefficient r_l^1 satisfies the relationship

$$r_l^1 = \int_{-\infty}^{\infty} \varphi(x - l)\, \frac{d}{dx}\, \varphi(x)\, dx, \qquad -38 \le l \le 38, \tag{C2}$$

where $\varphi(x)$ is a scaling function. The coefficients of the second order derivative operator can also be computed in the same way.